Cellular/Molecular

$\alpha_2\delta$-4 Is Required for the Molecular and Structural Organization of Rod and Cone Photoreceptor Synapses

Vasily Kerov,[1] Joseph G. Laird,[2] Mei-ling Joiner,[1] Sharmon Knecht,[7] Daniel Soh,[1] Jussara Hagen,[1] Sarah H. Gardner,[2] Wade Gutierrez,[3] Takeshi Yoshimatsu,[7] Sajag Bhattarai,[4] Teresa Puthussery,[8] Nikolai O. Artemyev,[1] Arlene V. Drack,[4] Rachel O. Wong,[7] Sheila A. Baker,[2,4] and Amy Lee[1,5,6]

[1]Department of Molecular Physiology and Biophysics, [2]Department of Biochemistry, [3]Medical Scientist Training Program, [4]Department of Ophthalmology and Institute for Vision Research, [5]Department of Otolaryngology-Head and Neck Surgery, [6]Department of Neurology, University of Iowa, Iowa City, Iowa 52242, [7]Department of Biological Structure, University of Washington, Seattle, Washington 98195, and [8]Casey Eye Institute, Oregon Health & Science University, Portland, Oregon 97239

$\alpha_2\delta$-4 is an auxiliary subunit of voltage-gated $Ca_v1.4$ L-type channels that regulate the development and mature exocytotic function of the photoreceptor ribbon synapse. In humans, mutations in the *CACNA2D4* gene encoding $\alpha_2\delta$-4 cause heterogeneous forms of vision impairment in humans, the underlying pathogenic mechanisms of which remain unclear. To investigate the retinal function of $\alpha_2\delta$-4, we used genome editing to generate an $\alpha_2\delta$-4 knock-out ($\alpha_2\delta$-4 KO) mouse. In male and female $\alpha_2\delta$-4 KO mice, rod spherules lack ribbons and other synaptic hallmarks early in development. Although the molecular organization of cone synapses is less affected than rod synapses, horizontal and cone bipolar processes extend abnormally in the outer nuclear layer in $\alpha_2\delta$-4 KO retina. In reconstructions of $\alpha_2\delta$-4 KO cone pedicles by serial block face scanning electron microscopy, ribbons appear normal, except that less than one-third show the expected triadic organization of processes at ribbon sites. The severity of the synaptic defects in $\alpha_2\delta$-4 KO mice correlates with a progressive loss of $Ca_v1.4$ channels, first in terminals of rods and later cones. Despite the absence of b-waves in electroretinograms, visually guided behavior is evident in $\alpha_2\delta$-4 KO mice and better under photopic than scotopic conditions. We conclude that $\alpha_2\delta$-4 plays an essential role in maintaining the structural and functional integrity of rod and cone synapses, the disruption of which may contribute to visual impairment in humans with *CACNA2D4* mutations.

Key words: Ca^{2+} channel; photoreceptor; retina; ribbon synapse; synaptogenesis

Significance Statement

In the retina, visual information is first communicated by the synapse formed between photoreceptors and second-order neurons. The mechanisms that regulate the structural integrity of this synapse are poorly understood. Here we demonstrate a role for $\alpha_2\delta$-4, a subunit of voltage-gated Ca^{2+} channels, in organizing the structure and function of photoreceptor synapses. We find that presynaptic Ca^{2+} channels are progressively lost and that rod and cone synapses are disrupted in mice that lack $\alpha_2\delta$-4. Our results suggest that alterations in presynaptic Ca^{2+} signaling and photoreceptor synapse structure may contribute to vision impairment in humans with mutations in the *CACNA2D4* gene encoding $\alpha_2\delta$-4.

Introduction

In the synaptic terminals of rod and cone photoreceptors (PRs), Ca^{2+} influx through voltage-gated Ca_v1 L-type Ca^{2+} channels triggers the release of glutamate required for the transmission of visual information through the retina (Schmitz and Witkovsky, 1997; Thoreson et al., 1997). Of the multiple classes of Ca_v1 channels, $Ca_v1.4$ is crucial for PR synaptic transmission and vision.

Received Dec. 12, 2016; revised May 10, 2018; accepted May 31, 2018.

Author contributions: V.K., M.-l.J., S.K., T.P., N.O.A., A.V.D., R.O.W., S.A.B., and A.L. designed research; V.K., J.G.L., M.-l.J., S.K., D.S., J.H., S.H.G., W.G., T.Y., S.B., T.P., N.O.A., and S.A.B. performed research; V.K., J.G.L., M.-l.J., S.K., J.H., W.G., T.Y., S.B., T.P., N.O.A., A.V.D., R.O.W., and S.A.B. analyzed data; S.A.B. and A.L. wrote the paper.

This work was supported by National Institutes of Health Grants NS084190 and DC009433 to A.L., EY026817 to A.L. and S.A.B., EY020542 and EY027054 to S.A.B., EY12682 to N.O.A., EY017168 to A.V.D., EY024265 to T.P., EY010572 to Ophthalmology Core Facility at Oregon Health & Science University, EY017101 to R.O.W., EY01730 Vision Core Grant to M. Neitz, RR018998 in support of the JEOL JEM transmission electron microscope in the Central Microscopy Research Facility, unrestricted grant from Research to Prevent Blindness to Oregon Health & Science University, Wynn Institute Advisory Board Grant to A.V.D., and Carver Research Program of Excellence Award to A.L. We thank William Paradee (University of Iowa Genome Editing Core) for aiding development of $\alpha_2\delta$-4 KO mice; Chantal Allamargot (University of Iowa Central Microscopy Research Facility) for processing of tissue samples for EM; David Wilson and John Ng (Oregon Health & Science University) for providing human retinal samples; Jordan Breffle, Taylor Vogel, and Jacqueline Gayet-Primo for excellent technical assistance; Ed Parker for serial TEM assistance; and Chris Johnson for assistance with measuring room luminescence.

The authors declare no competing financial interests.

Correspondence should be addressed to either of the following: Dr. Amy Lee, Department of Molecular Physiology and Biophysics, University of Iowa, 5318 PBDB, 169 Newton Road, Iowa City, IA 52242,

$Ca_v1.4$ channels are concentrated beneath the synaptic ribbon, a structure specialized for sustained exocytosis at the PR active zone (Mercer and Thoreson, 2011). Disruption of the *CACNA1F* gene encoding the pore-forming α_1 subunit (referred to hereafter as $Ca_v1.4$) blunts PR synaptic transmission in mice (Mansergh et al., 2005; Chang et al., 2006). Moreover, numerous mutations in *CACNA1F* cause human vision disorders, including X-linked congenital stationary night blindness Type 2 (Lodha et al., 2012) and cone-rod dystrophy (Jalkanen et al., 2006; Hauke et al., 2013).

In addition to their exocytotic function at mature PR synapses, $Ca_v1.4$ channels regulate the structure and molecular composition of the PR synapse. $Ca_v1.4$ knock-out (KO) mice lack synaptic ribbons and invaginating postsynaptic bipolar and horizontal cell processes that are characteristic of mature rod and cone synapses (Mansergh et al., 2005; Raven et al., 2008; Liu et al., 2013; Zabouri and Haverkamp, 2013; Regus-Leidig et al., 2014). In mice harboring an X-linked congenital stationary night blindness Type 2 mutation that greatly increases $Ca_v1.4$ Ca^{2+} influx, PR synapses are also lost (Knoflach et al., 2013, 2015; Liu et al., 2013; Regus-Leidig et al., 2014), indicating the importance of regulated $Ca_v1.4$ signaling for the maintenance of PR synapse structure and function.

Like other high-voltage-activated Ca_v channels, $Ca_v1.4$ channels interact with auxiliary β and $\alpha_2\delta$ subunits (Lee et al., 2015). Encoded by 4 different genes each, β and $\alpha_2\delta$ subunits generally increase the cell-surface density of Ca_v channels and can alter their biophysical properties (Dolphin, 2016). While genetic and immunohistochemical evidence supports a key role for the β_2 variant in $Ca_v1.4$ complexes in PR terminals (Ball et al., 2002, 2011; Katiyar et al., 2015; Lee et al., 2015), the importance of specific $\alpha_2\delta$ variants is less clear. $\alpha_2\delta$-1, 3, and 4 have been detected in the outer plexiform layer (OPL) containing PR synapses (De Sevilla Müller et al., 2013; Huang et al., 2013; Lee et al., 2015; Pérez de Sevilla Müller et al., 2015), but mRNA for $\alpha_2\delta$-4 far exceeds that of other $\alpha_2\delta$ variants in mouse retina (Knoflach et al., 2013). Moreover, mutations in the *CACNA2D4* gene encoding $\alpha_2\delta$-4 cause defects in cone-mediated vision in humans (Wycisk et al., 2006b; Ba-Abbad et al., 2016), and PR synapses are structurally and functionally disrupted in mice with a truncating mutation in *CACNA2D4* (Ruether et al., 2000; Wycisk et al., 2006a; Caputo et al., 2015). The mutation causes upregulation of a short splice variant of $\alpha_2\delta$-4 that cannot increase $Ca_v1.4$ current density like the full-length $\alpha_2\delta$-4 when heterologously coexpressed (Bacchi et al., 2015); it is not clear whether the retinal defects in the mutant mice are due to loss of function of the full-length protein or the abnormal properties of the short splice variant.

Here, we used genome editing to abolish $\alpha_2\delta$-4 expression in a new mouse line ($\alpha_2\delta$-4 KO). We find that $\alpha_2\delta$-4 is required to maintain the presynaptic density of $Ca_v1.4$ channels in rods and rod synapse structure, consistent with a report that was published while our study was under review (Wang et al., 2017). Additionally, we define a crucial role for $\alpha_2\delta$-4 in maintaining the architecture of cone synapses and their complement of $Ca_v1.4$ channels, the loss of which may explain the visual phenotypes in humans with *CACNA2D4* mutations.

Materials and Methods

Generation of $\alpha_2\delta$-4 KO mice. All procedures using mice were approved by the University of Iowa Institutional Animal Care and Use Committee. Guide RNAs (gRNAs) were generated by cloning sequences targeting exon 2 of the mouse *CACNA2D4* gene into separate px335 vectors (Cong et al., 2013): gRNA1f (5′-AACACGGTGACCAGATATTC) and gRNA1r (5′-CAGATTCCTGCCGAAGGTAT). The resulting vectors expressed the gRNAs and a nickase version of Cas9 (Cas9n). Correct targeting and nickase activity were confirmed by monitoring homology-guided repair of EGFP (Mashiko et al., 2013) in HEK293T cells cotransfected with the gRNA constructs and pEGxxFP plasmid containing exon 2 of *CACNA2D4*. gRNA constructs (2.5 ng/μl each) were injected into pronuclei of mouse zygotes (C57BL6 (RRID:IMSR_JAX:000664) × C57BL/6SJL(F1) (RRID:IMSR_JAX:100012)) by the University of Iowa Genome Editing Core Facility. Genotyping of resulting mouse pups was done by PCR (forward primer 5′-TATGAGTTAGATGCCTGCTTTGC, reverse primer 5′-TCACTGACCTTCTGCAGCAGG). Mice were backcrossed to the C57BL/6 parental strain for 2 or 3 generations. Males and females exhibited similar retinal and visual phenotypes, and so both sexes were used for experiments. C57BL6 (RRID:IMSR_JAX:000664) used as wild-type (WT) controls, $Ca_v1.4$ KO (RRID:IMSR_JAX:017761), and mGluR6 KO (nob3) (RRID:IMSR_JAX:016883) mice were obtained from The Jackson Laboratory.

Antibodies. The characterization of rabbit polyclonal $Ca_v1.4$ antibodies was described previously (Liu et al., 2013). Rabbit polyclonal $\alpha_2\delta$-4 antibodies were generated against a peptide corresponding to amino acids 784–799 (KVSDRKFLTPEDEASI) of mouse *CACNA2D4* (NP_001028554.2) by a commercial source (Covance). Antiserum was subject to affinity purification by standard protocols before use. The working concentrations of these and other antibodies are listed in Table 1.

Western blotting. For Western blots of transfected human embryonic kidney cells transformed with SV40 T-antigen (HEK 293T; American Type Culture Collection catalog #CRL-3216, RRID:CVCL_0063), cDNAs encoding hemagglutinin (HA) tagged $\alpha_2\delta$ variants were used. HA-$\alpha_2\delta$-1 (GenBank #NM_012919) in pMT2 was a kind gift from A. Dolphin. HA-$\alpha_2\delta$-2 was obtained from Addgene (#58731) and recloned into pcDNA3.1. HA was cloned into $\alpha_2\delta$-3 (in pMT2) between glycine 594 and lysine 595 (GenBank #NM_009785) using NEBuilder HiFi DNA Assembly cloning system. The HA epitope was inserted into human $\alpha_2\delta$-4 (in pcDNA 3.1) between leucine 505 and serine 506 (GenBank #NM_172364). All constructs were confirmed by DNA sequencing. HEK293T cells were transfected with cDNAs encoding HA-tagged $\alpha_2\delta$-1, $\alpha_2\delta$-2, $\alpha_2\delta$-3, or $\alpha_2\delta$-4 using GenePORTER transfection reagent (#T201015, Genlantis). After 48 h, transfected cells were processed for Western blot. Lysates from transfected cells were prepared and subjected to SDS-PAGE and Western blotting as described previously (Liu et al., 2013).

For Western blot analysis of retinal lysates, retinal tissue was harvested from 3-, 5-, or 21-week-old mice, lysed in buffer (20 mM HEPES, pH 7.4, 150 mM NaCl, 2 mM EGTA, 2 mM EDTA, 1% *n*-dodecyl β-S-maltoside) supplemented with protease inhibitor mixture and PMSF subjected to SDS-PAGE and transferred to PVDF membranes. Primary and secondary antibodies used for Western blot are listed in Table 1. For each experiment, the PVDF membrane was cut to allow for probing with actin antibodies. For quantitative analysis, chemiluminescent signals were collected with an Odyssey Fc Imaging System, and pixel intensity was measured with median background subtraction using Image Studio version 5.2 software. Signals were normalized to that for β actin from the same blot.

Immunofluorescent labeling of mouse and primate retina. Mice at P10 or older were killed with CO_2 followed by decapitation or cervical dislocation. At least 2 mice (male or female) were used for each genotype. Eyes were quickly removed and incubated in 4% PFA in 0.1 M phosphate buffer for 15–60 min. The anterior segments were removed, and the posterior eye cups were infiltrated with 30% sucrose on ice and frozen in embedding media on dry ice. Frozen blocks were cut in 12 μm sections, which were collected on electrostatic slides and stored at −80°C until use. Retinas from 2 adult (~13–15 years) female rhesus macaques (*Macaca mulatta*) and 1 adult (~7 years) cynomolgus macaque (*Macaca fascicularis*) were obtained from the Tissue Distribution Program at the Oregon

E-mail: amy-lee@uiowa.edu; or Dr. Sheila A. Baker, Department of Biochemistry, University of Iowa, 4-712 BSB, Iowa City, IA 52242, E-mail: sheila-baker@uiowa.edu.

Teresa Puthussery's present address: School of Optometry & Helen Wills Neuroscience Institute, University of California, Berkeley, CA 94720.

DOI:10.1523/JNEUROSCI.3818-16.2018

 0270-6474/18/386146-16$15.00/0

Table 1. Antibodies used for immunofluorescence or Western blot (WB)

Antibody	Source	Catalog	Concentration	RRID
Rabbit anti-$\alpha_2\delta$-4	In house (this paper)	NA	1:1000	NA (current study)
Rabbit anti-$Ca_v1.4$	In house (Liu et al., 2013)	NA	1:1000–1:4000	AB_2650487
Rabbit anti-Ribeye	Synaptic Systems	192103	1:1000	AB_2086775
Mouse anti-Ribeye	BD bioscience	612044	1:1000 1:500 (WB)	AB_399431
Mouse anti-PSD95	Thermo Fisher Scientific	MA1-046	1:1000	AB_2092361
Mouse anti-PSD-95	Millipore	529541	1:1000 (WB)	AB_565012
Rabbit anti-ERC 1b/2 (CAST)	Synaptic Systems	143003	1:2000 (WB)	AB_887715
Rabbit anti-synaptobrevin2 (VAMP2)	Synaptic Systems	104202	1:5000 (WB)	AB_887810
Rabbit anti-PKC-α	Santa Cruz Biotechnology	SC208	1:500	AB_2168668
PNA-AF647	Invitrogen	L32460	1:250	NA
Sheep anti-mGluR6	K. Martemyanov	NA	1:200	AB_2650490
Guinea pig anti-mGluR6	Neuromics	GP13105	1:500	AB_2341540
Mouse anti-GluR2	Millipore	MAB397	1:150	AB_11212990
Mouse anti-calbindin	Sigma-Aldrich	C9848-100UL	1:400	AB_476894
Rabbit anti-secretagonin	Biovendor	RD181120100	1:1000	AB_2034060
Mouse anti-HA	Covance	MMS-101R	1:1000 (WB)	AB_291263
Mouse anti-β-actin	Sigma-Aldrich	A2228	1:10 000 (WB)	AB_476697
AF488 goat anti-mouse	Thermo Fisher Scientific	A-11001	1:500	AB_2534069
AF568 goat anti-mouse	Thermo Fisher Scientific	A11004	1:500	AB_2534072
AF647 goat anti-mouse	Thermo Fisher Scientific	A-21235	1:500	AB_2535804
AF488 goat anti-rabbit	Thermo Fisher Scientific	A11008	1:500	AB_143165
AF568 goat anti-rabbit	Thermo Fisher Scientific	A-11011	1:500	AB_143157
AF647 goat anti-rabbit	Thermo Fisher Scientific	A-21244	1:500	AB_2535812
AF488 donkey anti-sheep	Thermo Fisher Scientific	A-11015	1:500	AB_2534082
AF647 donkey anti-sheep	Thermo Fisher Scientific	A-21448	1:500	AB_2535865
AF488 donkey anti-guinea pig	Thermo Fisher Scientific	A-11073	1:500	AB_2534117
Streptav-AF488	Thermo Fisher Scientific	S11223	1:500	AB_2336881
Biotin conjugate	Thermo Fisher Scientific	31820	1:500	AB_228340
HRP sheep anti-mouse IgG	GE Healthcare	NA931	1:20,000 (WB)	AB_772210
HRP donkey anti-rabbit IgG	GE Healthcare	NA934V	1:20,000 (WB)	AB_772206
AF594-WGA	Thermo Fisher Scientific	W11262	1:1000	NA

National Primate Research Center from animals used for unrelated experiments. Adult normal human retinal sections were obtained from surgical samples that were deidentified before investigator receipt. Use of these samples was thus deemed nonhuman subject research by the Oregon Health & Science University Institutional Review Board. Isolated primate retinas were fixed for 30 min in PFA and infiltrated in graded sucrose solutions (10%–30%) and frozen in embedding medium before obtaining tissue sections (14 μm) on a cryostat.

For immunofluorescence, tissue sections were incubated in blocking buffer (10% normal goat or donkey or horse serum and 0.5%–1% Triton X-100 diluted in PBS) for 30–60 min and then with primary antibodies for 1–24 h at room temperature or at 4°C. After rinsing 3 times with PBS/X-100, sections were incubated for 1 h in darkness in secondary antibodies (in some experiments with addition of Hoechst stain: #H6024, Sigma; 1:4000). All antibodies were diluted in PBS/X-100. For macaque and human tissues, antigen retrieval was performed before immunohistochemistry as described previously (Lee et al., 2015). Sections were rinsed 3 times, coverslipped, sealed with clear nail polish, and stored at 4°C. Confocal microscopy was performed using a Fluoview 1000 confocal microscope with 60× or 63× oil-immersion objectives (Olympus) or an LSM710 confocal microscope with a Plan-Neofluar 63×/1.4 oil-immersion objective (Carl Zeiss).

Quantitative analyses were performed on confocal images (maximum *z* stack projections) obtained from at least 3 animals per genotype. For quantitation of synapses, the number of RIBEYE-labeled structures adjacent to mGluR6 labeling was divided by the total number of RIBEYE-labeled structures. For quantitation of ribbons, confocal images were analyzed with ImageJ software by drawing a line through the long axis of the ribbon, the length of which was calibrated to the image scale bar. From each confocal image of retina labeled with RIBEYE and peanut agglutinin (PNA), 20 rod ribbons (not adjacent to PNA) were randomly selected for measurement by an investigator blinded to genotype. The area of cone pedicles (PNA labeling) in the same images was measured, and cone ribbons were counted as particles after applying the watershed algorithm. For quantitation of ectopic neurites and RIBEYE-labeling, neurites that extended from the OPL beyond the first layer of nuclei of the ONL were counted in the entire retinal section (sectioned through the optic nerve). For quantitation of $Ca_v1.4$ labeling, $Ca_v1.4$-labeled structures with or without PNA staining were counted in confocal images.

Analysis of retinal layer thickness. For confocal analysis, retinal cryosections were prepared as described for immunofluorescence but labeled with wheat germ agglutinin (Alexa 594) labeling was used to aid in visualization of the outer segment and synaptic layers. For quantitation, images were analyzed using Adobe Photoshop software. Hoechst-labeled nuclei were used to define the boundaries of each retinal layer, which was measured and calibrated to the image scale bar.

For optical coherence tomography (OCT), mice were anesthetized with ketamine/xylazine and kept warm on a heating pad. Tropicamide (1%) was used to dilate the pupils, and Genteal was added to keep the eye lubricated. Retinal images were collected with a Bioptigen spectral-domain imaging system (Bioptigen) equipped with a mouse retina objective, reference arm position set at 1264. Scan parameters were as follows: rectangular (1.4 mm^2) volume scans, 1000 A scans/B scan, 33 B scans/volume, 3 frames/B scan, and 1 volume. The outer nuclear layer was measured using Adobe Photoshop software to draw a line perpendicular to the layer from the outer limiting membrane to the OPL, the length of which was calibrated to the image scale bar.

Electron microscopy (EM). Eye tissue was processed as for immunofluorescence, except that eyes were fixed with 2.5% glutaraldehyde in 0.1 M cacodylate buffer, pH 7.2, for 1 h at 22°C and then were moved to 4°C. Eyecups were then dissected into smaller pieces and processed using standard protocols for embedding in epoxy resin (Eponate 812, Ted Pella). Retinas were oriented and cut into 70–80 nm sections. Sections were contrasted with 5% uranyl acetate in water followed by Reynold's lead citrate, and then imaged using JEOL JEM 1230 electron microscope at the University of Iowa Central Microscopy Research Facility.

Serial block face scanning EM was performed on $\alpha_2\delta$-4 KO mice and WT littermates at P19–P21. Retinal tissue was fixed in 4% glutaraldehyde in 0.1 M sodium cacodylate buffer for several hours. Thereafter, *en bloc* staining and tissue processing were performed as described previously (Della Santina et al., 2016). Serial sections were obtained every 50–65 nm, at 5 nm *x*, *y* resolution using the 3View system (Carl Zeiss; Gatan). TrackEM (National Institutes of Health) was used for visualization of the serial sections and to track individual ribbons across the sections.

In vivo *electroporation and Ca^{2+} imaging. In vivo* electroporation was done essentially as described previously (Matsuda and Cepko, 2004). Briefly, plasmid DNA (0.2–0.4 μl in sterile PBS: $\alpha_2\delta$-4/pcDNA3.1, ~3 μg/μl; pRho-mKate2, ~1 μg/μl) was injected into the subretinal space of newborn $\alpha_2\delta$-4 KO pups through the cornea with a Hamilton syringe with a 33-gauge blunt-ended needle. Tweezer-type electrodes were placed on the sides of the head, and five square pulses of 50 ms duration with 950 ms intervals were applied by using a pulse generator (ECM830, BTX). Pups were raised to adulthood for immunohistochemical analysis between the ages of P21 and P30.

For Ca^{2+} imaging experiments, WT, $\alpha_2\delta$-4 KO, or $Ca_v1.4$ KO mice were electroporated as described above but with pGP-CMV-GCaMP6s (Addgene) and pRho-synaptophysin-mRFP1 or pRho-mKate2 as electroporation markers. At P21–P30, the retina was dissected in oxygenated Ames medium (A1420, Sigma-Aldrich) prepared as per manufacturer instructions (with 1.9 g of sodium bicarbonate added) and gently flattened on a piece of nitrocellulose (BA85, Protran) with PRs facing up. After sectioning with a tissue slicer (51425, Stoelting), the slices (200 μm) were placed into a chamber constantly perfused with oxygenated physiological saline (in mM as follows: NaCl 119, $NaHCO_3$ 23, glucose 10, NaH_2PO_4 1.25, KCl 2.5, Na pyruvate 2, Na lactate 2, $CaCl_2$ 3, $MgCl_2$ [1 mM]) and imaged on a Fluoview 1000 confocal microscope (Olympus) with a 40× water-immersion objective at 512 × 512 resolution with 4× digital zoom. Fluorescent signals in the OPL were measured by perfusing with high K^+ solution (in mM as follows: NaCl 84, $NaHCO_3$ 23, glucose 10, NaH_2PO_4 1.25, KCl 40, Na pyruvate 2, Na lactate 2, $CaCl_2$ 3, $MgCl_2$ [1 mM]). For each recording, 75–120 total frames (2.2 s/frame) were obtained and analyzed in ImageJ. ROIs representing rod terminals were selected based on their position in the OPL and occasional connecting axon extending to a soma with typical rod morphology in the ONL. The fluorescence intensity in these ROIs (14 pixels in diameter) within electroporated rod terminals was recorded and analyzed as $Max\,\Delta F/F_o$, where $Max\,\Delta F$ is the difference between the maximum fluorescence signal ($Max\,F$) and the average fluorescence of the first five frames (F_o) collected before the application of high K^+ buffer. In some experiments, the tissue was incubated for 10 min with isradipine (#I6658, Sigma-Aldrich; 2 μM in physiological saline) before application of the high K^+ buffer also containing isradipine.

Electroretinography (ERG). ERG recordings were obtained for 5- to 6-week-old dark-adapted mice using the Espion E system (Diagnosys) as described previously (Liu et al., 2013). ERG responses were evoked in mice by a series of flashes ranging from 0.0001 to 100 cd · s/m^2. Responses to 6 sweeps were averaged for dim flashes up to 0.6 cd · s/m^2, 2 sweeps were averaged for 4 cd · s/m^2, and responses to brighter flashes were recorded without averaging. Intersweep intervals for flashes with increasing strength were increased from 10 to 60 s to allow full recovery from preceding flashes. To record photopic ERGs, mice were exposed to a background light (30 cd · s/m^2) for 3 min before flash stimulation (3, 30, or 100 cd · s/m^2). Six sweeps were averaged.

For flicker response assays, mice were dark-adapted overnight and anesthetized with an intraperitoneal injection of ketamine (87.5 mg/kg) and xylazine (2.5 mg/kg). ERGs were recorded simultaneously from the corneal surface of each eye after pupil dilation (1% tropicamide) using gold ring electrodes (Diagnosys) referenced to a needle electrode (The Electrode Store) placed on the back of the head. Another needle electrode placed in the tail served as ground. A drop of hypromellose (0.3%) was placed on the corneal surface to ensure electrical contact and to maintain corneal integrity. Body temperature was maintained at a constant temperature of 38°C using the system's heating pad. All stimuli were presented in a Ganzfeld (ColorDome, Diagnosys), and the mouse head and electrode positioning was monitored on the camera attached to the system. Dim red light was used for illumination until testing was completed.

Table 2. Serial block face scanning EM analysis of cone synaptic triads in WT and $\alpha_2\delta$-4 KO mice[a]

Genotype	Cone number	Ribbon + triad	Total
WT	1	7	10
	2	7	11
	3	8[b]	9
$\alpha_2\delta$-4 KO	1	2	13
	2	4	10
	3	1	6
	4	5	12

[a]Data were obtained from cone synapses reconstructed in the OPL of WT and $\alpha_2\delta$-4 KO at P19. "Ribbon + triad" was scored when ribbon was vertically aligned at a junction between two processes with a third in between. "Total" represents the total number of ribbons in the reconstructed cone pedicle ($n = 3$ pedicles in WT, $n = 4$ pedicles in $\alpha_2\delta$-4 KO, 1 mouse each).

[b]One ribbon contacted 2 triads.

A flicker protocol as previously described (Tanimoto et al., 2016) with some modification was used to obtain the recordings. Briefly, flashes of fixed luminance (3 cd · s/m^2) but varying frequencies (0.5–30 Hz) were used during recording. No background illumination was used, and the responses were averaged 15 times.

Visually guided behavioral assay. Mice (male and female, 1- to 7-month-old mice) were trained to swim in a 4-foot-diameter pool to a high-contrast visible escape platform measuring 4 inches in diameter, ~0.5 inch above the water line. A series of 5 trials are conducted per day. After 4 d of training trials, test trials are conducted over 6 d (for a total of 30 trials) and the average time to escape recorded. For scotopic testing, the same animals tested under photopic conditions were dark-adapted overnight before completing another 6 d of trials.

Experimental design and statistical analysis. Western blots of transfected cell lysates were performed at least 3 times and used untransfected cells as controls (see Fig. 1). Western blots of mouse retinal lysate were performed at least 3 times using 4 retinas/genotype for each experiment. Immunofluorescence of WT and $\alpha_2\delta$-4 KO mouse retina with $\alpha_2\delta$-4 antibodies and PNA was performed at least 3 times and involved analysis of 4 retinal sections/experiment (2 mice/experiment). $\alpha_2\delta$-4 immunolabeling was analyzed in 21 sections from 3 macaque eyes in 3 experiments and in 15 sections in 3 human eyes in 2 experiments. For these experiments, the $\alpha_2\delta$-4 immunolabeling was deemed specific based on its similarity with the labeling pattern in mouse retina and that it was never observed in past negative control experiments when the same secondary antibodies were used alone.

Analysis of retinal layer thickness in fluorescently labeled retinal sections involved 60 measurements from 3 images for each of 3 animals per genotype (see Fig. 2). For OCT, 15–40 measurements of retinal layer thickness were taken from 3 images collected from the center of the eye (near the optic nerve) in 2–6 mice for each age group.

Analyses of rod ribbon length and RIBEYE:mGluR6 clusters were performed on 9 images taken from 3 retinal sections taken from each of 3 mice per genotype (8 or 9 retinal images analyzed/mouse) (see Fig. 3).

The number of neurites and RIBEYE puncta extending into the ONL was determined in 2 retinal sections from each of 3 mice per genotype (see Fig. 4).

Reconstructions of cone pedicles were performed from one retina each from 3 WT and 4 $\alpha_2\delta$-4 KO mice at P19-P21 (see Fig. 5; Table 2).

The number of $Ca_v1.4$ puncta in the OPL was determined in 6 images taken from 2 retinal sections from each of 3 mice per age group per genotype (see Fig. 6; Table 3).

Western blots of mouse retinal lysate collected from animals at 5 weeks of age were performed 6 times using 4 retinas/genotype for each experiment (see Fig. 7).

Ca^{2+} imaging measurements were made on 2 or 3 retinal slices from one retina from each mouse (3–5 mice per genotype) (see Fig. 8).

ERGs were performed on 5–7 animals per genotype. Flicker response assays were performed on 4 WT, 4 $Ca_v1.4$ KO, and 9 $\alpha_2\delta$-4 KO mice (see Fig. 9).

Swim assays were performed using 5 WT, 3 $\alpha_2\delta$-4 heterozygous (HET), 6 $\alpha_2\delta$-4 KO, 6 $Ca_v1.4$ KO, and 5 mGluR6 KO mice around the same time of day by the same investigator (see Fig. 10).

Table 3. Quantification of $Ca_v1.4$ immunofluorescence in the OPL[a]

	Rod			Cone		
Age/genotype	$Ca_v1.4$-labeled structures, median (95% CI)	*n*	*p*	$Ca_v1.4$-labeled structures, median (95% CI)	*n*	*p*
P10						
HET	42.0 (29.8, 52.3)	4	0.0048	3.0 (2, 4)	15	0.024
$\alpha_2\delta$-4 KO	5.5 (3.5, 7.2)	6		2.0 (1, 3)	15	
P14						
HET	58.5 (54.4, 74.3)	6	0.0004	2.5 (2, 3)	26	<0.0001
$\alpha_2\delta$-4 KO	2.0 (1.3, 4.2)	9		1.0 (0, 1)	29	
P21						
HET	82.0 (66.8, 98.2)	4	0.0048	4.0 (3, 5)	19	<0.0001
$\alpha_2\delta$-4 KO	0.5 (−0.19, 1.5)	6		0 (0, 0)	27	
$Ca_v1.4$ KO	0 (0, 0)	6	0.1818	0 (0, 0)	15	>0.9999

[a]The number of $Ca_v1.4$-labeled structures in the OPL of HET, $\alpha_2\delta$-4 KO, and $Ca_v1.4$ KO mice at the indicated ages were counted in confocal micrographs processed for immunofluorescence as in Figure 7. $Ca_v1.4$ labeling was assigned to rods or cones based on the presence or absence, respectively, of PNA fluorescence. *n* = number of animals. *p* values were determined by Mann–Whitney test.

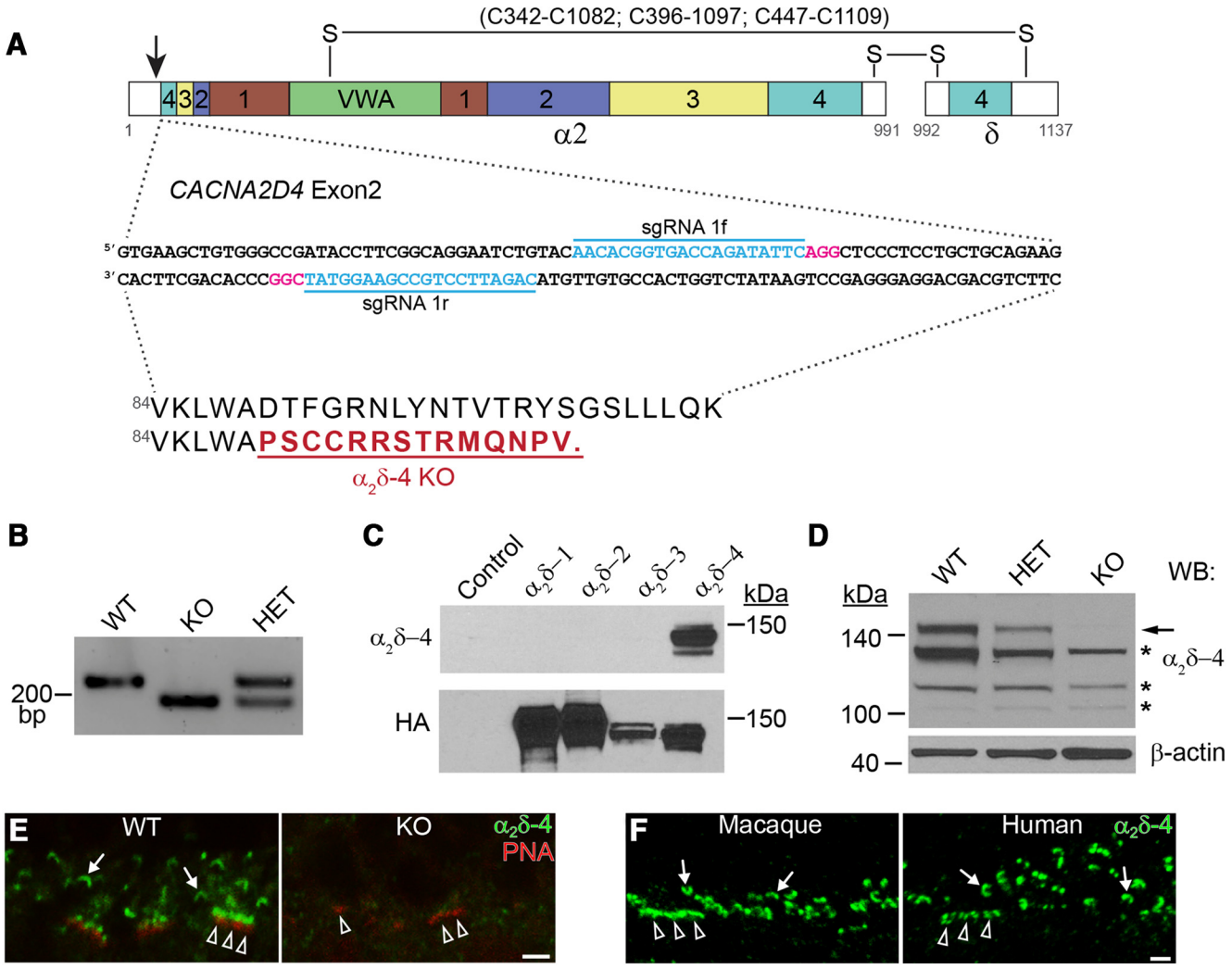

Figure 1. Generation of $\alpha_2\delta$-4 KO mice. ***A***, Schematic illustrating domain structure of $\alpha_2\delta$-4 and strategy for interrupting exon 2 using the indicated guide RNA sequences (sgRNA 1f and 1r). The four chemosensory domains (1–4) are indicated in colored boxes. VWA, von Willebrand A domain. Numbers beneath diagram indicate amino acids. Putative disulfide bonds (S-S) between α_2 and δ are shown above the diagram. The resulting amino sequence change (underlined) and premature truncation are shown below. ***B***, PCR with primers flanking the deleted region in exon 2 using retinal genomic DNA from WT, KO, and HET mice. ***C***, ***D***, Western blots probed with $\alpha_2\delta$-4 or HA antibodies of lysates from HEK293T cells untransfected (control) or transfected with HA-tagged $\alpha_2\delta$ variants (***C***) or retina from WT, HET, or KO mice (***D***). Arrow and asterisks indicate specific and nonspecific protein detection, respectively. ***E***, ***F***, Confocal micrographs showing labeling with $\alpha_2\delta$-4 antibodies in WT and $\alpha_2\delta$-4 KO mouse retina at P21 (***E***) and macaque and human retina (***F***). ***E***, Mouse retina was double-labeled with fluorescent PNA to mark cone terminals. $\alpha_2\delta$-4 labeling is present at ribbons of rods (arrows) and cones (arrowheads). Scale bars, 2 μm.

Statistical differences were determined using GraphPad Prism software (version 6 or 7). Statistical significance was defined using an α of 0.05. Normality was assessed by the Shapiro–Wilk test. Parametric data were analyzed by ANOVA or *t* test; nonparametric data were analyzed by Kruskal–Wallis test or Mann–Whitney test.

Results

Generation of $\alpha_2\delta$-4 KO mice and $\alpha_2\delta$-4 antibodies

To prevent expression of all functionally relevant domains of $\alpha_2\delta$-4, we introduced a stop codon in exon 2 of the mouse

CACNA2D4 gene encoding $\alpha_2\delta$-4 using clustered regularly interspaced short palindromic repeats (CRISPR) and CRISPR-associated protein 9n (Cong et al., 2013) (Fig. 1*A*). The presence of the mutant allele (c.360_408 del) in HET and homozygous mice was verified by genotyping (Fig. 1*B*). The resulting homozygous mice were of normal body weight and size and showed no overt behavioral phenotypes.

To confirm the absence of $\alpha_2\delta$-4 protein in the homozygous mice, we generated rabbit polyclonal antibodies against an epitope in $\alpha_2\delta$-4 that is not conserved in other $\alpha_2\delta$ variants. These antibodies were specific for the $\alpha_2\delta$-4 isoform because they recognized a band of the predicted molecular weight of the glycosylated form of $\alpha_2\delta$-4 (~140 kDa) in Western blots of lysates of HEK293T cells transfected with HA-tagged $\alpha_2\delta$-4 but not with the other three HA-tagged $\alpha_2\delta$ variants; the expression of each was confirmed by detection with HA antibodies (Fig. 1*C*). The $\alpha_2\delta$-4 antibodies detected a ~140 kDa band in retinal lysate from WT mice that was weaker in HET mice and absent in homozygous $\alpha_2\delta$-4 KO mice (Fig. 1*D*). Additional bands were labeled but were deemed nonspecific because they were present in all 3 genotypes. In the OPL of WT mice, immunolabeling was associated with elongated structures resembling synaptic ribbons in terminals of rods and cones, the latter of which were labeled with fluorescent PNA (Fig. 1*E*). Only very weak punctate immunofluorescence was seen in the OPL of $\alpha_2\delta$-4 KO mice (Fig. 1*E*). The pattern of $\alpha_2\delta$-4 localization at rod and cone synapses in macaque and human retina was similar to that in WT mouse retina (Fig. 1*F*). Together, these results verify that $\alpha_2\delta$-4 protein is not expressed in the retina of our $\alpha_2\delta$-4 KO mouse line and support the specificity of our $\alpha_2\delta$-4 antibodies for Western blot and immunofluorescence. Our findings also provide the first evidence that $\alpha_2\delta$-4 is localized in rod and cone terminals in primate retina, thus corroborating genetic evidence for the importance of $\alpha_2\delta$-4 in PR transmission in humans (Wycisk et al., 2006b).

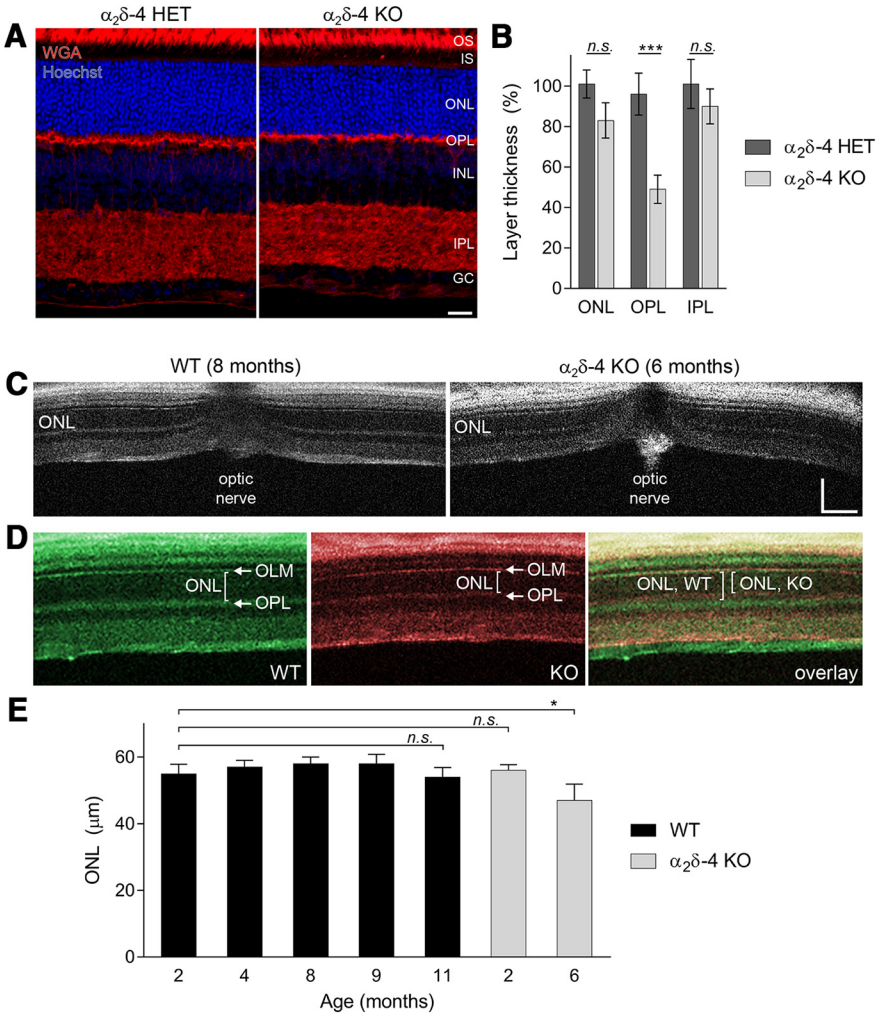

Figure 2. PR synapse organization is disrupted in $\alpha_2\delta$-4 KO mice. ***A***, Sections of $\alpha_2\delta$-4 HET and $\alpha_2\delta$-4 KO retina at P21 stained with wheat germ agglutinin, to label the membrane rich outer segment and synaptic layers, and Hoechst to label the nuclei. OS, Outer segment; IS, inner segment; ONL, outer nuclear layer; INL, inner nuclear layer; IPL, inner plexiform layer; GC, ganglion cell layer. Scale bar, 20 μm. ***B***, Quantification of the thickness of retinal layers in histological sections processed in ***A***. Data were normalized to HET values. ***C***, OCT scans from WT (8-month-old) and $\alpha_2\delta$-4 KO (2-month-old) retinas. Position of optic nerve is indicated. Scale bar, 100 μm. ***D***, Pseudocolored OCT scans of WT and $\alpha_2\delta$-4 KO retina at higher magnification. Brackets indicate ONL thickness defined by the boundaries of the outer limiting membrane (OLM) and the OPL (arrows). ***E***, Quantification of ONL thickness as measured in OCT scans in ***C***, ***D*** in WT and $\alpha_2\delta$-4 KO retinas at the indicated ages. ***B***, ***D***, Data are mean ± SD. Significant differences were determined by one-way ANOVA with Sidak's *post hoc* test in ***B*** and one-way ANOVA with Dunnett's *post hoc* test in ***E***. n.s., not significant ($p > 0.05$). *$p \leq 0.05$, ***$p \leq 0.001$.

$\alpha_2\delta$-4 KO mice undergo a late-onset retinal degeneration

We investigated the consequences of genetic silencing of $\alpha_2\delta$-4 first by histology. In mature $\alpha_2\delta$-4 KO mice at 2 months of age, the OPL was significantly thinner than in HET control littermates (47% thinner, 95% CI [26, 67]; adjusted $p = 0.0001$; Fig. 2*A*,*B*). There was a trend toward thinning of the ONL at this age in $\alpha_2\delta$-4 KO mice, but it was not statistically significant (18% thinner compared with HET, 95% CI [−3, 39]; adjusted $p = 0.95$). The difference in the thickness of the inner plexiform layer of $\alpha_2\delta$-4 KO mice compared with HET mice was also not significant (11% thinner, 95% CI [−10, 32]; adjusted $p = 0.42$), suggesting that bipolar cell synapses with ganglion and amacrine cells are not grossly altered in the complete absence of $\alpha_2\delta$-4. We also used optical coherence tomography to collect retinal images of living WT and $\alpha_2\delta$-4 KO mice. In 6-month-old $\alpha_2\delta$-4 KO mice, the major layers of the retina were readily observed, and there were no gross disruptions in retinal structure compared with 8-month-old WT mice (Fig. 2*C*). The average ONL thickness (57 μm, 95% CI [56, 58]) was not significantly different between WT mice from 2 to 11 months of age (mean $\Delta = 3$ μm, 95% CI [−11.2, 5.2]; adjusted $p = 0.79$). Compared with WT mice, the ONL was significantly thinner (~15%; mean $\Delta = 8$ μm, 95% CI [−0.28, 15.72]; adjusted $p = 0.04$) in 6-month-old but not 2-month-old $\alpha_2\delta$-4 KO mice (mean $\Delta = 1$ μm, 95% CI [−9.63, 7.63]; adjusted $p = 1.00$; Fig. 2*D*,*E*). These results show that $\alpha_2\delta$-4 KO mice undergo a mild retinal degeneration after 2 months of age.

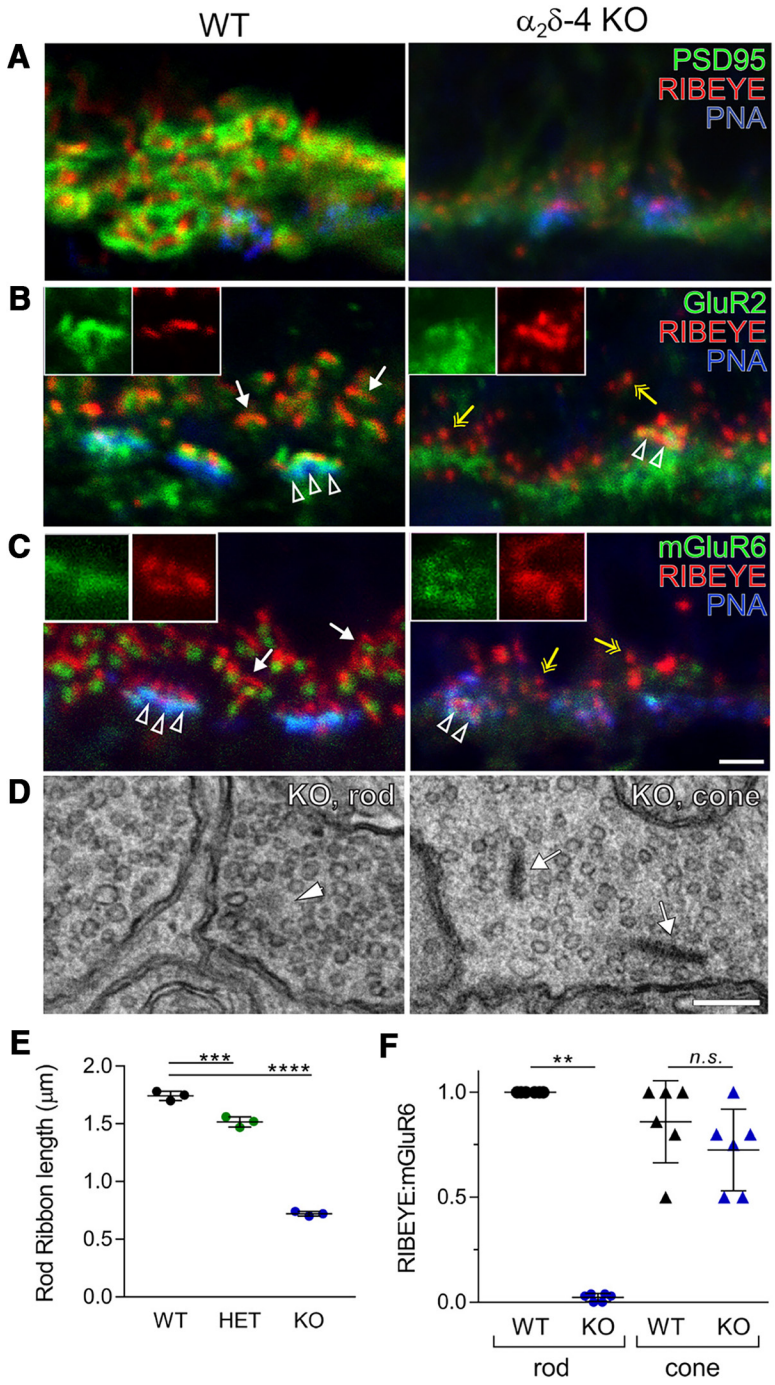

Figure 3. PR synapses are abnormal in $\alpha_2\delta$-4 KO mice. ***A–C***, Confocal micrographs of the OPL of WT and $\alpha_2\delta$-4 KO retina at P21 triple-labeled with PNA and antibodies against RIBEYE and PSD95 (***A***), GluR2 (***B***), or mGluR6 (***C***). RIBEYE labeling associated with rods (white arrows) and cones (arrowheads). Yellow arrows indicate punctate RIBEYE labeling in $\alpha_2\delta$-4 KO retina. Insets, Higher magnification of cone synapse labeling. Scale bar, 2 μm. ***D***, Electron micrographs showing ribbon sphere (left, arrowhead) found in rods, and ribbons in cones (right, arrows) in $\alpha_2\delta$-4 KO retinas. Scale bar, 200 nm. ***E***, ***F***, Quantitative analyses of rod ribbon lengths (***E***) and fraction of total RIBEYE punctate adjacent to mGluR6 punctate in rods or cones (***F***). Significant differences were determined by one-way ANOVA with Tukey's *post hoc* test in ***E*** and Mann–Whitney in ***F***. Data are mean ± SD. n.s., not significant ($p > 0.05$). $^{**}p \leq 0.01$, $^{***}p \leq 0.001$, $^{****}p \leq 0.0001$.

PR synapses are abnormal in $\alpha_2\delta$-4 KO mice

To determine whether the thinning of the OPL in $\alpha_2\delta$-4 KO mice (Fig. 2*A*,*B*) resulted from a loss of PR synapses, we triple-labeled retinal sections with antibodies against various synaptic proteins and PNA to label cone pedicles. We restricted analysis to mice at P21 to avoid confounding effects of PR degeneration in older $\alpha_2\delta$-4 KO mice (i.e., >2 months old). Labeling for RIBEYE, the major ribbon protein, was more spherical than elongated in $\alpha_2\delta$-4 KO than in WT retina (Fig. 3*A*–*C*). In addition, labeling for the scaffolding protein PSD95, which lines the presynaptic membrane of rods and cones, was strongly diminished in $\alpha_2\delta$-4 KO retina (Fig. 3*A*). Postsynaptic proteins were also affected based on double-labeling with antibodies against glutamate receptors on processes of horizontal cells (GluR2) and depolarizing (ON) bipolar cells (mGluR6). Unlike in WT retina, punctate labeling for GluR2 and mGluR6 was generally not clustered with RIBEYE labeling in $\alpha_2\delta$-4 KO, except in PNA-positive cone pedicles (Fig. 3*B*,*C*).

By TEM, ribbons were observed in cone pedicles, whereas only electron-dense spheres were detected in rod spherules of $\alpha_2\delta$-4 KO mice (Fig. 3*D*). Resembling structural intermediates of ribbons during assembly (Regus-Leidig et al., 2009) and disassembly (Spiwoks-Becker et al., 2004), these spheres likely corresponded to the RIBEYE-labeled puncta in $\alpha_2\delta$-4 KO retina (Fig. 3*A*–*C*) and were significantly shorter in rod terminals compared with RIBEYE-labeled ribbons in WT mice (mean $\Delta = 1$ μm, 95% CI [0.93, 1.12]; adjusted $p < 0.0001$; Fig. 3*E*). Rod ribbons were slightly but significantly shorter in HET than in WT mice (mean $\Delta = 0.23$ μm, 95% CI [0.13, 0.32]; adjusted $p = 0.007$; Fig. 3*E*), which may result from the decreased levels of $\alpha_2\delta$-4 protein in the retina of HET compared with WT mice (Fig. 1*D*). To estimate the number of synapses, we measured the fraction of total RIBEYE-labeled structures that were adjacent to mGluR6 labeling. Compared with WT mice, this metric was significantly lower in $\alpha_2\delta$-4 KO rods (mean $\Delta = 0.97$, 95% CI [0.96, 1]; $p = 0.0022$) but not in $\alpha_2\delta$-4 KO cones (mean $\Delta = 0.16$, 95% CI [−0.14, 0.5]; adjusted $p = 0.22$; Fig. 3*F*). Together, these results verify that the absence of $\alpha_2\delta$-4 impacts the presynaptic organization of rod PRs.

Distinct alterations in rod and cone synapse structure in $\alpha_2\delta$-4 KO mice

The outgrowth of processes from bipolar cells and horizontal cells from the OPL and appearance of ectopic synapses in the ONL are common to mice with presynaptic defects in PRs (Spiwoks-Becker et al., 2004). To determine whether this is the case in $\alpha_2\delta$-4 KO retina, we performed double-labeling with antibodies against RIBEYE and calbindin or protein kinase Cα (PKC) to mark horizontal cells and rod bipolar cells, respectively, or against secretagogin, a Ca^{2+} binding protein expressed in most types of cone ON and OFF bipolar cells

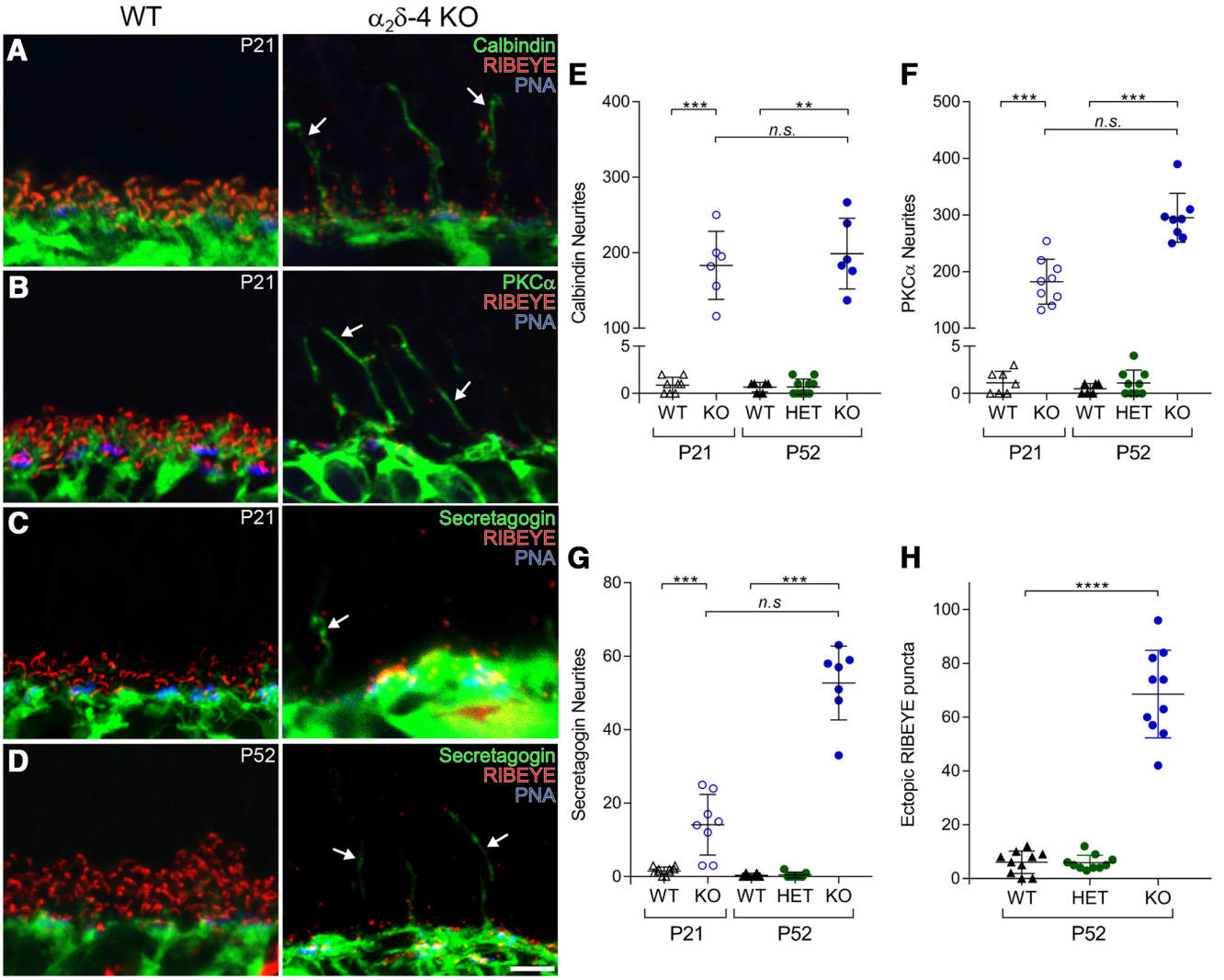

Figure 4. Ectopic ribbons and sprouting of horizontal and bipolar cell processes in $\alpha_2\delta$-4 KO retina. ***A–D***, Confocal micrographs of WT and $\alpha_2\delta$-4 KO retina labeled with PNA and antibodies against RIBEYE and calbindin (***A***), PKCα (***B***), or secretagogin (***C***, ***D***) at P21 (***A–C***) or P52 (***D***). Arrows indicate processes of horizontal cells (***A***), rod bipolar cells (***B***), and cone bipolar cells (***C***, ***D***) extending from the OPL. Scale bar, 5 μm. ***E–G***, Quantification of the number of neurites extending into the ONL from images. ***H***, Quantification of RIBEYE-labeled structures in the ONL. ***E–G***, Significant differences between WT and $\alpha_2\delta$-4 KO at P21 were determined by Mann–Whitney test; significant differences between all groups regardless of age were determined by Kruskal–Wallis test and Dunn's *post hoc* test. ***H***, Data were analyzed by one-way ANOVA and Tukey's *post hoc* test. Data are plotted as mean ± SD. n.s., not significant ($p > 0.05$). $^{**}p \leq 0.01$, $^{***}p \leq 0.001$, $^{****}p \leq 0.0001$.

(Puthussery et al., 2010). At both P21 and P52, calbindin-, PKC-, and secretagogin-labeled processes terminated in the OPL in WT retina but extended into the ONL in $\alpha_2\delta$-4 KO retina (Fig. 4*A–D*). Compared with WT mice, there was a significant increase in the number of neurites immunolabeled for calbindin (median Δ = 188, 95% CI [154, 200], $p = 0.0007$ at P21; median Δ = 186, 95% CI [137, 266], $p = 0.002$ at P52; Fig. 4*E*), PKC (median Δ = 182, 95% CI [140, 218], $p = 0.0002$ at P21; median Δ = 292, 95% CI [259, 310], $p = 0.0007$ at P52; Fig. 4*F*), and secretagogin (median Δ = 13, 95% CI [3, 22], $p = 0.0002$ at P21; median Δ = 57, 95% CI [47, 59], $p = 0.001$ at P52; Fig. 4*G*). Compared with WT and HET mice, RIBEYE-labeled puncta were more numerous in the ONL of $\alpha_2\delta$-4 KO (median Δ = 63, 95% CI [52, 74]; adjusted $p <$ 0.0001; Fig. 4*H*). Thus, remodeling of rod and cone bipolar neurites occurs along with their presynaptic partners in $\alpha_2\delta$-4 KO retina.

Despite the presence of morphologically normal cone ribbons (Fig. 3*D*), the sprouting of cone bipolar neurites (Fig. 4*C*, *D*, *G*) indicated a significant disruption of cone synapse organization. To investigate this further, we analyzed cone synapses in retina from $\alpha_2\delta$-4 KO and control mice by serial block face scanning EM. We traced the cone pedicles and all processes apposed to the ribbons. In 3D reconstructions of pedicles of both WT and $\alpha_2\delta$-4 KO cones, the number of ribbons was not significantly different (mean = 10 in each, $p = 0.9$ by t test; Fig. 5*A*). While ribbons in both WT and $\alpha_2\delta$-4 KO cone pedicles were always associated with the pedicle membrane (i.e., not floating), the arrangement of postsynaptic processes appeared different between genotypes (Fig. 5*B*, *C*). In WT pedicles, ribbons were most often observed at "triad-like" structures where the ribbon aligned vertically at the active zone and was flanked by three processes that invaginated into the cone pedicle at the base of the ribbon (examples of two ribbon sites shown in Fig. 5*B*, *C*, WT). There were no significant differences in the number of ribbons or their positioning at synaptic triads in WT and HET cone pedicles (Fig. 5-1, available at https://doi.org/10.1523/JNEUROSCI.3818-16.2018.f5-1). In contrast, the fraction of ribbons that were present at synaptic triads was significantly less in $\alpha_2\delta$-4 KO cones (0.28 ± 0.07) compared

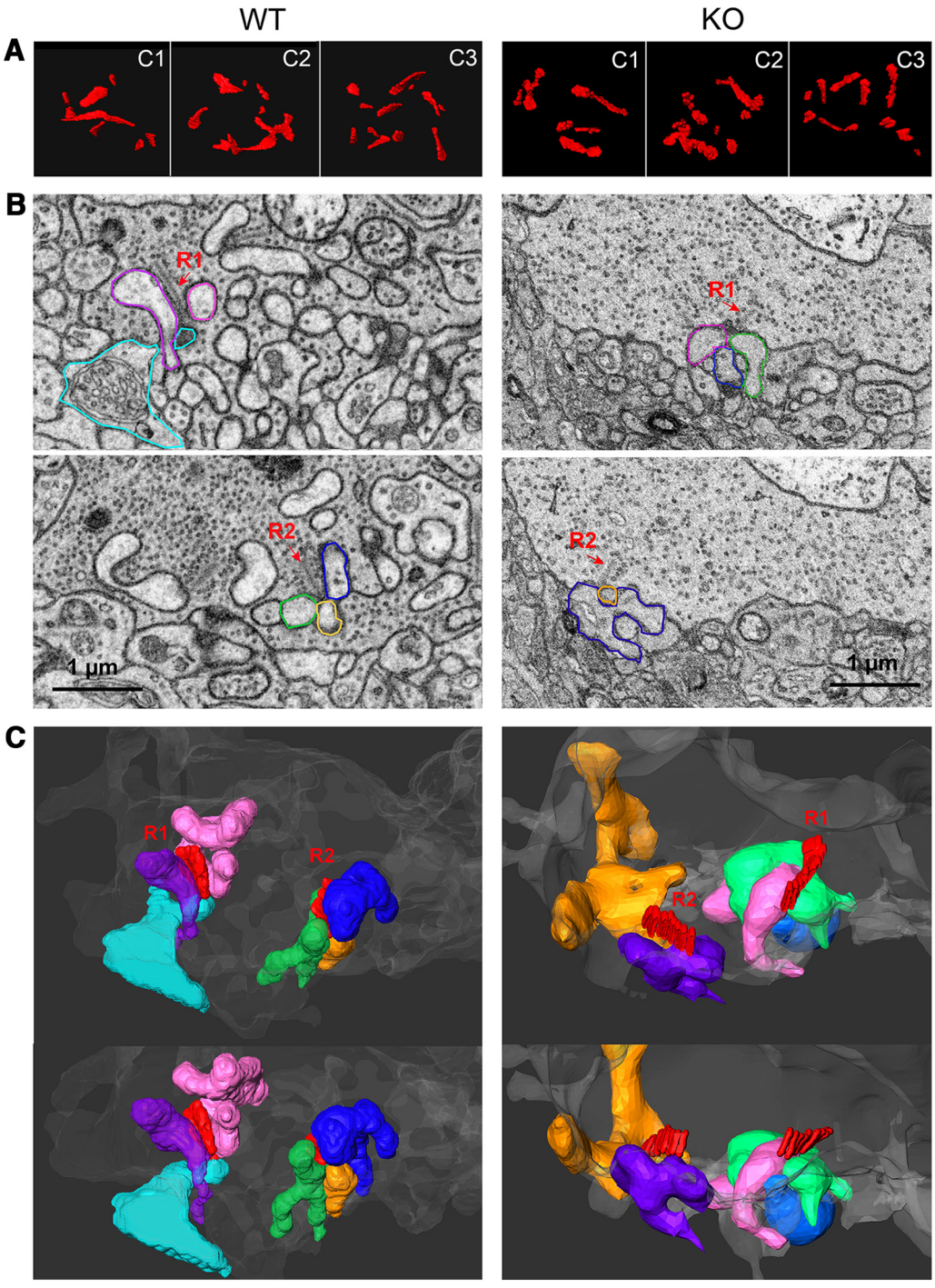

Figure 5. Aberrant synaptic organization of cone synapses in $\alpha_2\delta$-4 KO mice determined by serial block face scanning EM. ***A***, Examples of ribbons traced from sections through 3 cone pedicles (c1–c3) from WT and $\alpha_2\delta$-4 KO retina. ***B***, Two image planes (top, bottom) of a WT (left) or KO (right) cone pedicle each with 2 ribbons (R1, R2). Processes that contact the cone at these ribbon sites are pseudocolored. Each process was traced to some distance from the ribbon site to provide a 3D view of the synaptic arrangement at the ribbon site. ***C***, Two 3D views (top, bottom) of the processes colored in ***B*** and their associated ribbon (R1, R2). Left, In the WT pedicle, typical triad-like arrangements are observed at both ribbon (R1, R2) sites, as evidenced by three processes converging at the ribbon site. The identities of these processes are not confirmed because of their partial reconstructions. Similar results were obtained in reconstructions of HET cone pedicles (Fig. 5-1, available at https://doi.org/10.1523/JNEUROSCI.3818-16.2018.f5-1). Right, In the KO pedicle, triadic arrangement of processes at the ribbon sites was not readily apparent. The R1 ribbon terminated opposite two processes (magenta, green), with a third (blue) somewhat further away. The R2 ribbon was apposed to only two processes (orange, purple), and did not appear "sandwiched" by these two processes, as typically seen in WT triads.

with WT cones (0.74 ± 0.08, $p = 0.008$ by t test; Table 2). Often only two processes terminated in the pedicle right at the base of the ribbon in $\alpha_2\delta$-4 KO cone pedicles (Fig. 5*C*). Similar results were obtained in 3D reconstructions of images obtained by TEM (data not shown). Although the processes apposed to any of the ribbons could not be identified without further tracing to their cell of origin, they likely arose from horizontal and bipolar cells based on our immunofluorescent detection of their processes improperly extending into the ONL of $\alpha_2\delta$-4 KO retina (Fig. 4*A*, *C*). Together, our results revealed imperfect synaptic

arrangements at $\alpha_2\delta$-4 KO cone synapse arrangements that is more evident postsynaptically than presynaptically.

The levels of presynaptic $Ca_v1.4$ channels and synaptic proteins are reduced in $\alpha_2\delta$-4 KO retina

$\alpha_2\delta$ proteins enhance the cell-surface trafficking and presynaptic abundance of Ca_v channels (Hoppa et al., 2012; Cassidy et al., 2014). Considering that $Ca_v1.4$ channels are required for the formation and maintenance of ribbons in rods and cones (Raven et al., 2008; Liu et al., 2013; Zabouri and Haverkamp, 2013; Regus-Leidig et al., 2014), the less severe disruption of ribbons in cones than in rods of $\alpha_2\delta$-4 KO mice could reflect greater preservation of presynaptic $Ca_v1.4$ channels in cone pedicles than in rod spherules. To test this, we analyzed the distribution of synaptic $Ca_v1.4$ channels and ribbons in $\alpha_2\delta$-4 KO mice by double-label immunofluorescence with $Ca_v1.4$ antibodies and PNA at different postnatal ages using HET littermates as controls.

As we described previously in WT retina (Liu et al., 2013), $Ca_v1.4$ labeling in HET retina was associated with RIBEYE spheres at P10 (Fig. 6*A*) and tightly colocalized with ribbons at P14 and P21 (Fig. 6*B*,*C*). In $\alpha_2\delta$-4 KO retina, punctate $Ca_v1.4$ labeling was very sparse at P10 and P14 (Fig. 6*A*,*B*). At P21, there was no difference in $Ca_v1.4$ labeling in $\alpha_2\delta$-4 KO and the background immunofluorescence seen in $Ca_v1.4$ KO retina (Fig. 6*C*,*D*; Table 3). In rod terminals of $\alpha_2\delta$-4 KO mice, $Ca_v1.4$ labeling was greatest at P10 but $<$13% of that in HET mice at any age examined. $Ca_v1.4$ labeling was also lost in $\alpha_2\delta$-4 KO cones, but more slowly than in rods. The number of $Ca_v1.4$-labeled cone terminals was significantly less in the OPL of $\alpha_2\delta$-4 KO mice than HET mice and became undetectable with age (Fig. 6*A*–*C*; Table 3). Electroporation of cDNA encoding $\alpha_2\delta$-4 in the retina of neonatal (P0) $\alpha_2\delta$-4 KO mice rescued the loss of presynaptic $Ca_v1.4$ channels and ribbons in rod terminals (Fig. 6*E*). This approach restricts expression of the exogenous $\alpha_2\delta$-4 to rods because cones have differentiated at this age and therefore resist transfection (Matsuda and Cepko, 2004). Nevertheless, these results show that, at rod synapses, $\alpha_2\delta$-4 expression presynaptically is necessary for maintaining the density of $Ca_v1.4$ channels and ribbon structure.

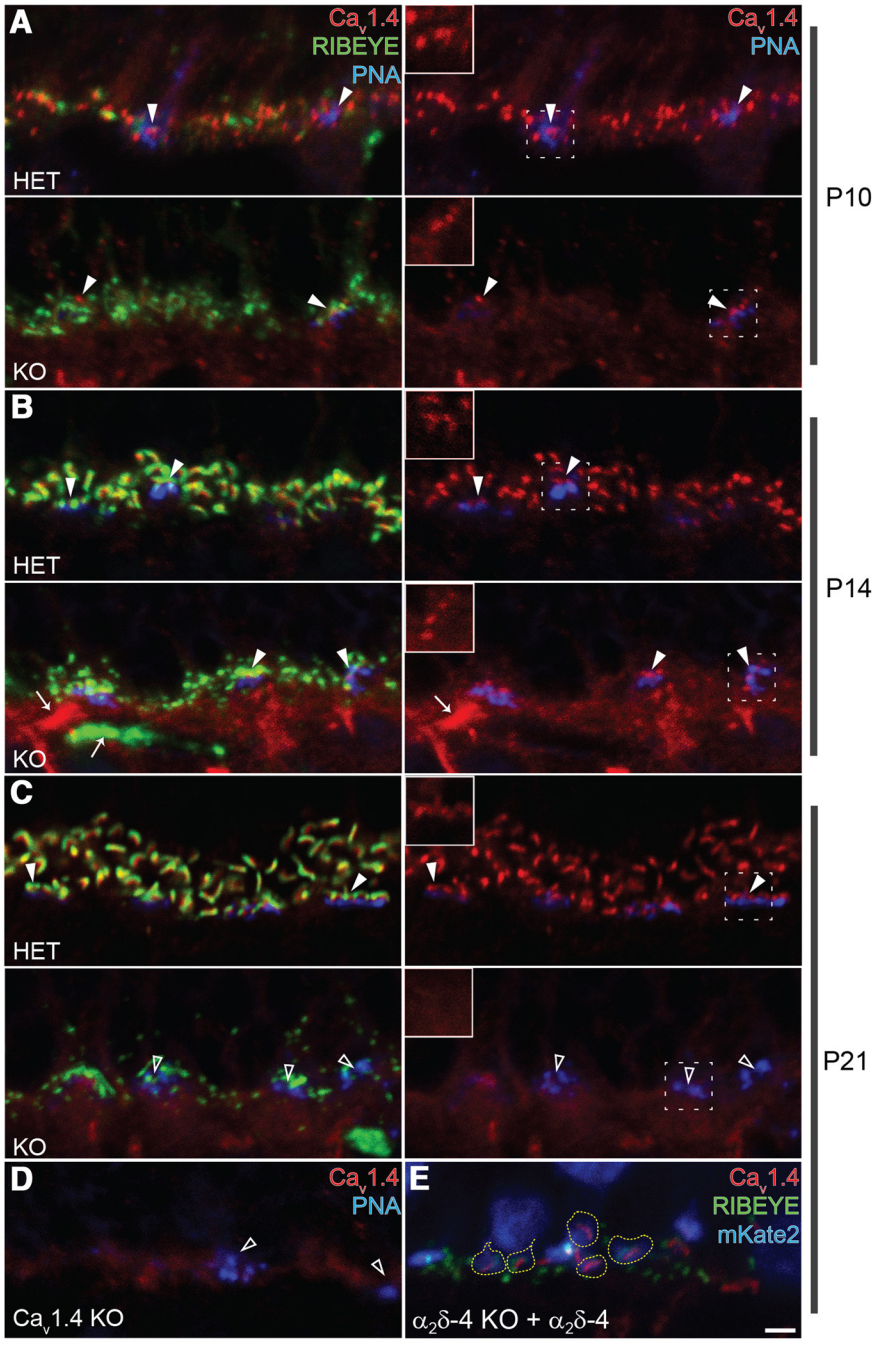

Figure 6. $Ca_v1.4$ immunofluorescence declines faster in terminals of rods than cones in the OPL of $\alpha_2\delta$-4 KO retina. ***A–C***, Confocal micrographs of the OPL of HET (top) and $\alpha_2\delta$-4 KO (bottom) or mouse retina labeled with PNA and antibodies against RIBEYE and $Ca_v1.4$ at the indicated postnatal ages; for clarity, the images in the right column are the same as those on the left but shown without the RIBEYE channel. ***D***, Confocal micrograph of the OPL of $Ca_v1.4$ KO mouse retina labeled with PNA and $Ca_v1.4$. Examples of cone terminals with (filled arrowheads) or without (open arrowheads) clusters of $Ca_v1.4$ labeling are marked. Insets, Higher-magnification views of the cone terminals in the area indicated by the dashed box. ***E***, OPL of $\alpha_2\delta$-4 KO retina electroporated with $\alpha_2\delta$-4 and the electroporation marker mKate2, and immunostained with RIBEYE and $Ca_v1.4$ antibodies. mKate2-labeled synaptic terminals are encircled with yellow dotted lines. ***B***, Arrows indicate nonspecific staining. Quantitation of $Ca_v1.4$ immunofluorescence in ***A–D*** is in Table 3. Scale bar, 2 μm.

It should be noted that our $Ca_v1.4$ antibodies are likely of limited sensitivity in fixed tissue because they require very weak fixation conditions in mouse retina (i.e., 4% PFA for 15 min). Therefore, our immunofluorescence analysis may under-report the levels of $Ca_v1.4$ in $\alpha_2\delta$-4 KO retina. Indeed, the antibodies detected a faint band on Western blots of retinal lysates from $\alpha_2\delta$-4 KO mice at 5 weeks of age (Fig. 7*A*). The absence of this band in $Ca_v1.4$ KO mice confirmed the specificity of the $Ca_v1.4$ signal. In semiquantitative analyses, the level of $Ca_v1.4$ in $\alpha_2\delta$-4 KO retina was significantly reduced to only ~20% of that in WT

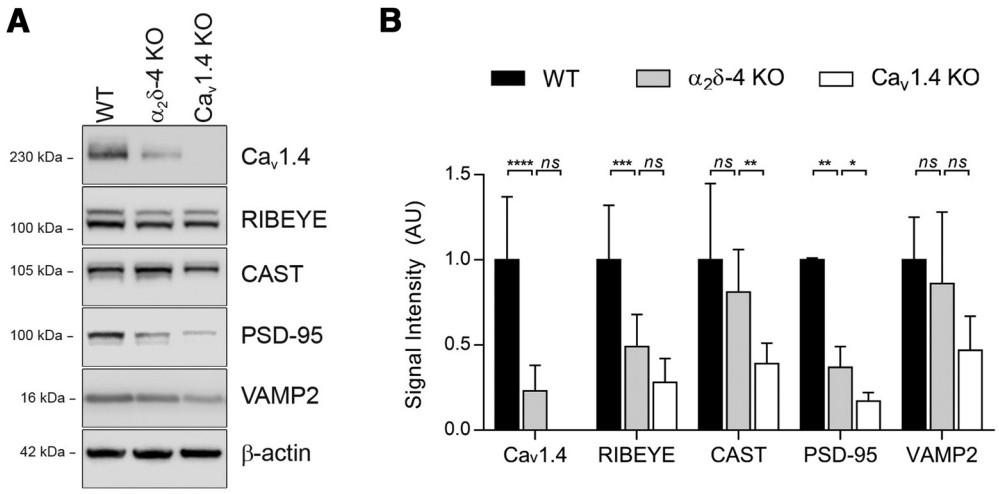

Figure 7. The levels of $Ca_v1.4$ and other presynaptic proteins are decreased in $\alpha_2\delta$-4 KO retina. ***A***, Representative Western blots of retinal lysates from WT, $\alpha_2\delta$-4 KO, and $Ca_v1.4$ KO mice at 5 weeks of age. ***B***, Quantitative analysis of results in ***A***. Signal intensity represents Western blot signals normalized to that for β-actin (***B***). Data are mean ± SD. Significant differences were determined by one-way ANOVA with Dunnett's *post hoc* test. n.s., not significant ($p > 0.05$). *$p \leq 0.05$, **$p \leq 0.01$, ***$p \leq 0.001$, ****$p \leq 0.0001$.

retina (mean $\Delta = 1.708$ AU, 95% CI [2.415, 1.002], adjusted $p = 0.0001$; Fig. 7*B*). These results indicate a severe loss of $Ca_v1.4$ channels from PR terminals in $\alpha_2\delta$-4 KO retina.

Because key presynaptic proteins are disrupted in $Ca_v1.4$ KO PR terminals (Raven et al., 2008; Liu et al., 2013; Zabouri and Haverkamp, 2013; Regus-Leidig et al., 2014), we next tested whether the level of presynaptic PR proteins was similarly disturbed in $\alpha_2\delta$-4 KO and $Ca_v1.4$ KO retina by Western blot. Consistent with our immunofluorescence analysis (Fig. 3*A*,*B*), the level of RIBEYE and PSD-95 protein in $\alpha_2\delta$-4 KO compared with WT retina was reduced by ~50% by Western blot (Fig. 7*A*,*B*). However, the levels of the active zone-associated structural protein (CAST) and vesicle associated membrane protein-2 (VAMP2) were not significantly different from WT (Fig. 7*A*,*B*). Although the levels of CAST in $Ca_v1.4$ KO retina have not been investigated, our findings of reduced levels of RIBEYE and PSD-95, but not VAMP2, in $\alpha_2\delta$-4 KO retina are similar to what occurs in $Ca_v1.4$ KO retina (Raven et al., 2008; Liu et al., 2013; Zabouri and Haverkamp, 2013; Regus-Leidig et al., 2014), and therefore may be a consequence of downregulation of $Ca_v1.4$ in $\alpha_2\delta$-4 KO retina.

To functionally confirm the reductions in the density of presynaptic $Ca_v1.4$ channels in $\alpha_2\delta$-4 KO PR terminals, we measured Ca^{2+} signals by confocal imaging in rods of mice in which the genetically encoded Ca^{2+} indicator, GCaMP6s, was expressed by electroporation. Under basal conditions, GCaMP6s signals were only detected in cells considered to be rods based on their morphology and localization of soma in the ONL and synaptic terminals in the OPL, and occasionally visible axon connecting the two (Fig. 8*A*). The level of baseline GCaMP6s fluorescence varied between cells but was not significantly different between genotypes ($p = 0.0548$ by ANOVA, $F_{(2,12)} = 3.735$). This variability is unlikely to be a factor in depolarization-evoked GCaMP6s signals, which are not affected by differences in GCaMP6s expression levels (Lock et al., 2015). Depolarization with a high concentration of K^+ caused robust increases in GCaMP6s fluorescence in terminals that could be clearly distinguished from the rod soma and axon by their size and position in the OPL (Fig. 8*A*). The Ca^{2+} signals in the WT rod terminals were likely mediated by $Ca_v1.4$ channels because they were blocked by the Ca_v1 antagonist isradipine (Fig. 8*B*), reduced in $\alpha_2\delta$-4 KO mice, and absent in $Ca_v1.4$ KO mice (Fig. 8*C*). The maximal change in GCaMP6s fluorescence normalized to baseline signal (Max $\Delta F/F_o$) was significantly weaker in rod terminals of $\alpha_2\delta$-4 KO mice (median = 0.16, 95% CI [0.07, 0.31]) than in WT mice (median = 4.25, 95% CI [3.8, 4.76]; adjusted $p < 0.0001$) but was significantly greater than in $Ca_v1.4$ KO rods (median = 0.03, 95% CI [0.01, 0.08]; adjusted $p = 0.043$; Fig. 8*C*). These results demonstrate an essential role for $\alpha_2\delta$-4 in maintaining functional $Ca_v1.4$ channels in PR synaptic terminals.

Electroretinograms (ERGs) are abnormal in $\alpha_2\delta$-4 KO mice

Given that the $Ca_v1.4$ function is reduced, but not completely abolished, in $\alpha_2\delta$-4 KO PR terminals, we expected abnormalities in PR synaptic transmission to be less severe than those exhibited by $Ca_v1.4$ KO mice. We tested this in ERGs of 2-month-old, dark-adapted mice in response to a single-flash luminance series. As shown previously (Mansergh et al., 2005; Regus-Leidig et al., 2014), b-waves representing transmission from PRs to depolarizing (ON) rod and cone bipolar cells were significantly reduced in $Ca_v1.4$ KO compared with WT mice (mean $\Delta = 408$ μV, 95% CI [383, 432]; adjusted $p < 0.0001$; see Fig. 10*A*,*B*). Although slightly larger in HET mice than in WT mice (mean $\Delta = -33$ μV, 95% CI [−57, −9]; adjusted $p = 0.003$), b-wave amplitudes were strongly reduced in $\alpha_2\delta$-4 KO and were not significantly different from those in $Ca_v1.4$ KO mice (mean $\Delta = -6$ μV, 95% CI [−30, 19]; adjusted $p = 0.93$; Fig. 9*A*,*B*). Also similar to $Ca_v1.4$ KO mice, there was a small but significant reduction in the amplitude of the a-wave in $\alpha_2\delta$-4 KO mice compared with WT (mean $\Delta =$ 75 μV, 95% CI [55, 95]; adjusted $p < 0.0001$; Fig. 9*B*). As the a-wave reflects light-dependent hyperpolarization of PRs, these results are consistent with the trend toward thinning of the ONL in 2-month-old $\alpha_2\delta$-4 KO mice (Fig. 2) but unlikely to account for the complete absence of b-waves in these mice.

An electronegative ERG may be a consequence of presynaptic or postsynaptic dysfunction in ON (rod and cone) and/or OFF (cone) bipolar pathways. The source of the deficit can be partially discriminated in flicker response assays in which retinal responses are evoked by flashes of fixed luminance (3 cd·s/m^2) but varying frequencies (0.5–30 Hz). Responses in the low-frequency range reflect signaling principally by the primary rod pathway, in the mid-range by the cone ON-bipolar pathway, and in the high-

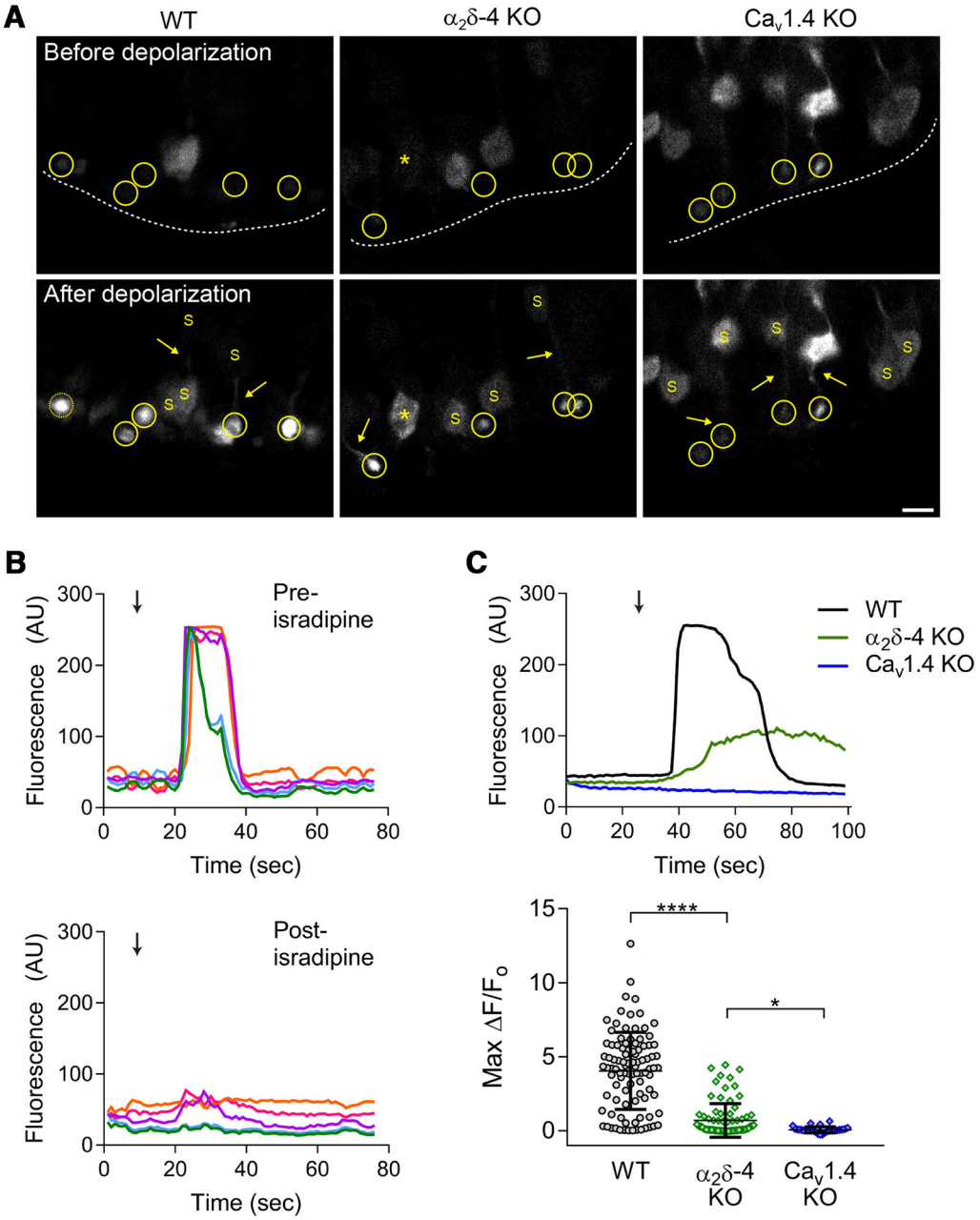

Figure 8. Presynaptic Ca^{2+} signals in rod spherules are diminished in $\alpha_2\delta$-4 KO mice. ***A***, Representative images of GCaMP6s signals in the retina of electroporated WT, $\alpha_2\delta$-4 KO, and $Ca_v1.4$ KO mice before (top) and after (bottom) exposure to high K^+-containing solution. Top, Dashed line indicates the boundary of the OPL. Rod terminals serving as ROIs (circled) were readily distinguished from rod soma (S). Rod axons (arrows) and occasionally soma (*) showed increases in K^+-evoked signals (bottom). Scale bar, 5 μm. ***B***, Representative traces from WT mice corresponding to GCaMP6s fluorescence following exposure to high K^+. Arrow indicates initiation of 10 s perfusion with 40 mM K^+ before (top) and after (bottom) 10 min perfusion with isradipine (2 μM). The color of the trace represents an individual ROI and is the same in the preisradipine and postisradipine traces. ***C***, Top, Representative traces corresponding to changes in GCaMP6s fluorescence evoked as in ***B***, but in WT, $\alpha_2\delta$-4 KO, $Ca_v1.4$ KO mice. Bottom, Maximal change in GCaMP6s fluorescence (Max $\Delta F/F_o$) in response to high K^+ in synaptic terminals of WT, $\alpha_2\delta$-4 KO, and $Ca_v1.4$ KO mice. Error bars indicate mean ± SD. Significant differences were determined by Kruskal–Wallis test with Dunnett's *post hoc* test. *$p \leq 0.05$, ****$p \leq 0.0001$.

frequency range by the cone OFF-bipolar pathway (Tanimoto et al., 2016). Compared with WT controls, flicker responses in $\alpha_2\delta$-4 KO mice were significantly weaker across all stimulus frequencies (mean Δ = 122 μV, 95% CI [107, 137]; adjusted $p <$ 0.0001). There was no difference in flicker responses in $\alpha_2\delta$-4 KO and $Ca_v1.4$ KO mice (mean Δ = 9 μV, 95% CI [−5, 24]; adjusted p = 0.26; Fig. 9*C*,*D*). Therefore, both ON and OFF bipolar pathways are impaired $\alpha_2\delta$-4 KO mice, and to a similar extent as in $Ca_v1.4$ KO mice.

Visual behavior is significantly affected in $\alpha_2\delta$-4 KO mice

ERGs reflect the properties of neuronal activity in the visual pathway, but not necessarily whether vision is preserved. To determine whether visual function is affected in $\alpha_2\delta$-4 KO mice, we used a behavioral task in which mice are trained to swim in a pool to a visible escape platform; the latency to swim to the platform in subsequent trials reflects visual function (Prusky et al., 2000; Pang et al., 2006). Following an initial training period, WT, HET, and $\alpha_2\delta$-4 KO mice learned to swim to the platform (Fig. 10*A*,*B*).

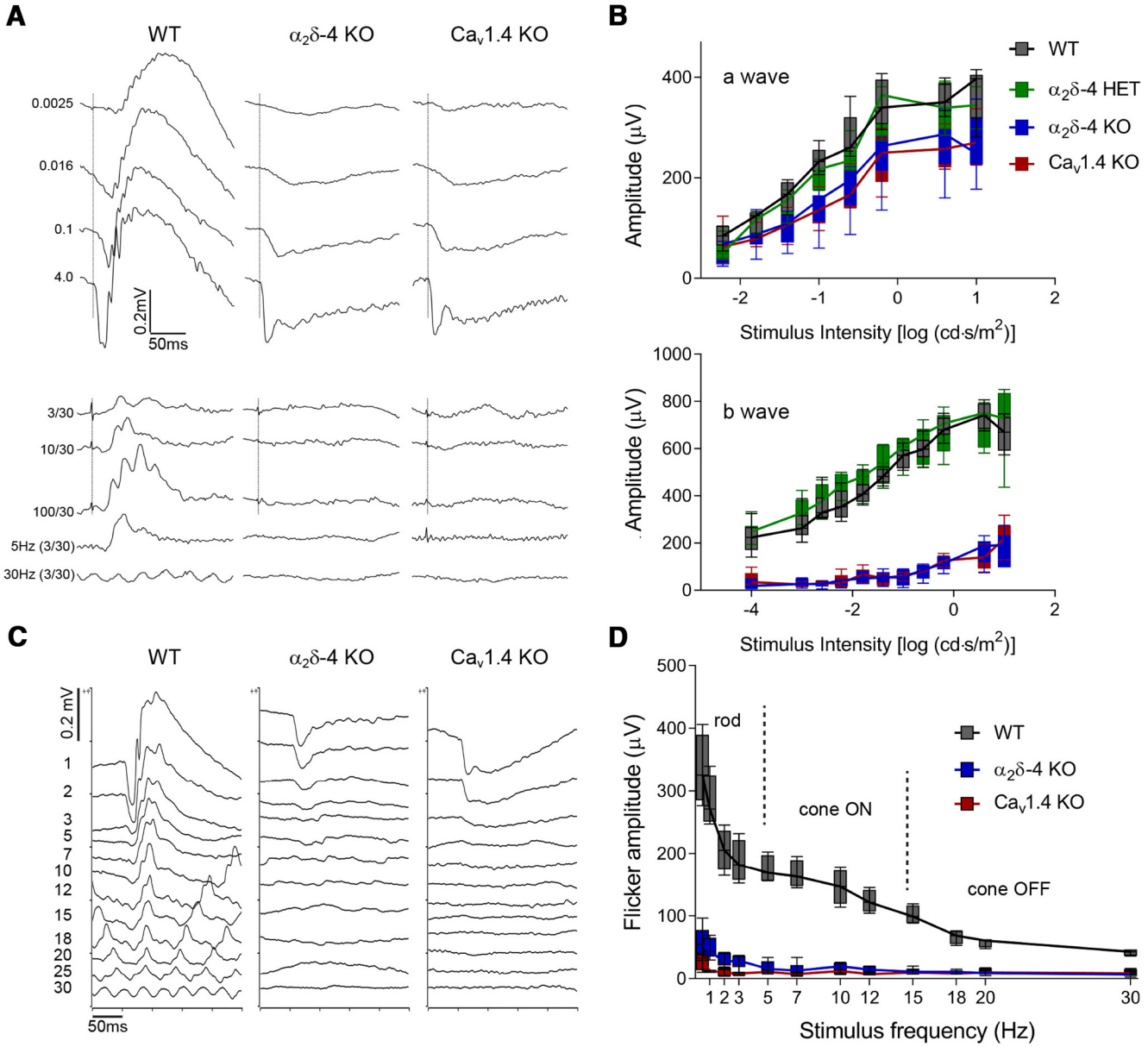

Figure 9. b-waves are undetectable in ERGs of $\alpha_2\delta$-4 KO mice. ***A***, Representative traces of scotopic (top) and photopic (bottom) ERGs from WT, $\alpha_2\delta$-4 KO, and $Ca_v1.4$ KO mice. Flash intensities shown at left in cd · s/m^2. Photopic traces represent responses to flashes delivered in the presence of background light of 30 cd · s/m^2. ***B***, Box-and-whisker plots of a-wave and b-wave amplitudes from WT, $\alpha_2\delta$-4 HET, $\alpha_2\delta$-4 KO, and $Ca_v1.4$ KO mice; $n = 6$ mice/genotype. ***C***, ***D***, Representative traces of flicker responses (***C***) and box-and-whisker plots of flicker amplitudes plotted against flash frequency (***D***) in WT ($n = 4$), $\alpha_2\delta$-4 KO ($n = 9$), and $Ca_v1.4$ KO ($n = 4$) mice. The dominant signaling pathway driving the response at each range of frequencies separated by dashed lines is indicated. ***B***, ***D***, Data are plotted with boxes set at 25th–75th, and whiskers at 5th-95th, percentiles about the median, and analyzed by two-way ANOVA and Dunnett's or Tukey's *post hoc* tests.

Consistent with ERG analyses (Fig. 9*A*,*B*), there was no difference in how fast WT and HET mice found the platform in normal room lighting (photopic, luminance of 11.1 cd/m^2) or in dim light (scotopic, luminance of 0.002 cd/m^2; Fig. 10*C*). Under scotopic conditions where mice are dependent on the primary rod pathway, $\alpha_2\delta$-4 KO mice performed significantly worse than WT and HET mice (mean $\Delta = 21.8$ s, 95% CI [15.3, 28.3]; adjusted $p = 0.0001$) but significantly better than $Ca_v1.4$ KO mice (mean $\Delta = 21.7$ s, 95% CI [15.5, 27.9]; adjusted $p = 0.0001$). This was surprising given the similar abnormalities in ERGs of $\alpha_2\delta$-4 KO and $Ca_v1.4$ KO mice (Fig. 9). Moreover, under photopic conditions where both rod and cone pathways can operate, $\alpha_2\delta$-4 KO mice behaved similarly to WT mice (mean $\Delta = -2.3$ s, 95% CI [−8.7, 4.2]; adjusted $p = 0.78$; Fig. 10*C*). Again, this was unexpected given the major structural defects in cone synapses in $\alpha_2\delta$-4 KO mice (Fig. 5).

In trying to reconcile these inconsistencies, we considered that visual behavior could be guided by alternate pathways in mutant mouse strains that show similar ERGs but differ in their retinal and visual phenotypes (McCall and Gregg, 2008). For example, mice lacking expression of mGluR6 (mGluR6 KO) perform normally in a visual learning assay despite the expectation that light-evoked signaling through ON pathways should be strongly impaired (Masu et al., 1995). To assess the range of visual deficits uncovered by the swim assay, we compared the swim times of $\alpha_2\delta$-4 KO mice with those of mGluR6 KO mice. Similar to $\alpha_2\delta$-4 KO mice, mGluR6 KO mice exhibited impairment under scotopic, but not photopic, conditions

(Fig. 10*C*). These results suggest that the swim assay can accurately report visual behavior associated with complete loss of PR synapse structure and function (i.e., $Ca_v1.4$ KO) but not in mice with less severe deficits in these parameters (e.g., $\alpha_2\delta$-4 KO, mGluR6 KO).

Discussion

Here, we show that $\alpha_2\delta$-4 is required for maintaining the density of presynaptic $Ca_v1.4$ channels in PRs and the molecular and structural organization of both rod and cone synapses. In $\alpha_2\delta$-4 KO mice, ribbon abnormalities are greater and $Ca_v1.4$ channels are lost faster in terminals of rods than in cones. These defects likely contribute to the lack of b-waves in ERGs and alterations in visual behavior in $\alpha_2\delta$-4 KO mice. Our results highlight the importance of the $Ca_v1.4$ channel complex in the regulation of PR synapse structure and function.

A necessary role for $\alpha_2\delta$-4 as a $Ca_v1.4$ channel subunit

Although all $\alpha_2\delta$s increase the current density of Ca_v channels in heterologous expression systems (Bacchi et al., 2015; Dolphin, 2016), their effect in regulating the trafficking of native Ca_v channels varies with channel and cell type. In hippocampal neurons in culture, alterations in the expression of $\alpha_2\delta$ influence the number of presynaptic $Ca_v2.1$ channels and neurotransmitter release properties (Hoppa et al., 2012). At the mouse inner hair cell synapse of $\alpha_2\delta$-2 null mice, the presynaptic localization of $Ca_v1.3$ is unchanged despite significant reductions in $Ca_v1.3$ current density (Fell et al., 2016). By contrast, we find that $\alpha_2\delta$-4 is essential for clustering of presynaptic $Ca_v1.4$ channels at PR ribbons. $\alpha_2\delta$-4 is not absolutely required for the forward trafficking of $Ca_v1.4$ to the PR terminal because $Ca_v1.4$ immunofluorescence is found in the OPL early in development (Fig. 6; Table 3) and Ca^{2+} signals are measurable in PR terminals of $\alpha_2\delta$-4 KO retina (Fig. 8*C*). Like other $\alpha_2\delta$ variants (Bourdin et al., 2015), $\alpha_2\delta$-4 may enhance the stability of $Ca_v1.4$ channels in PR terminals by suppressing their turnover. The reduced amounts of appropriate synaptic scaffolds, such as PSD-95 in $\alpha_2\delta$-4 KO retina (Figs. 3*A*, 7), may further limit retention of $Ca_v1.4$ channels in the presynaptic membrane. The loss of $Ca_v1.4$ channels and correct positioning of other presynaptic as well as postsynaptic proteins (e.g., mGluR6, Fig. 3*F*) may contribute to the severe disruption of ERG responses in $\alpha_2\delta$-4 KO mice (Fig. 9).

Defects in rod and cone synapse structure in $\alpha_2\delta$-4 KO mice

Considering that the formation of synaptic ribbons in PRs requires $Ca_v1.4$ (Raven et al., 2008; Liu et al., 2013; Zabouri and Haverkamp, 2013; Regus-Leidig et al., 2014), the ribbon defects in $\alpha_2\delta$-4 KO mice are not surprising. Notably, the reductions in $Ca_v1.4$ protein and ribbon abnormalities in $\alpha_2\delta$-4 KO mice are identical to those in mice lacking expression of the $Ca_v\beta_2$ subunit (β_2-KO). Like $\alpha_2\delta$, $Ca_v\beta$ subunits increase the cell-surface density of Ca_v channels (for review, see Buraei and Yang, 2013). Thus, reductions in $Ca_v1.4$-mediated Ca^{2+} influx and subsequently weak exocytotic function may stall ribbon morphogenesis in β_2-KO and $\alpha_2\delta$-4 KO rod terminals. In agreement with this possibility, ribbon abnormalities are also seen in rods under conditions of artificially high intraterminal Ca^{2+} buffering (Regus-Leidig et al., 2010) and in PRs that lack proteins involved in

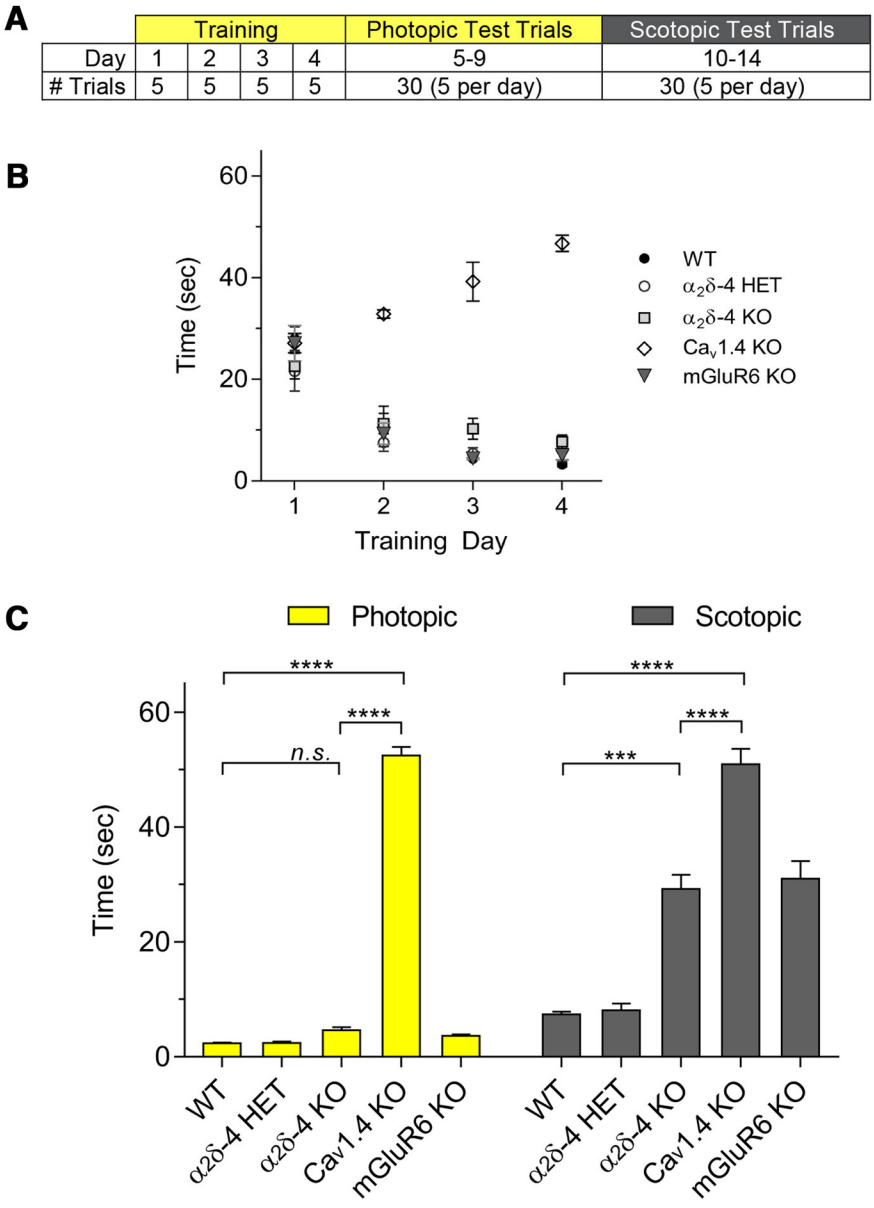

Figure 10. Dim-light vision is compromised in $\alpha_2\delta$-4 KO mice. ***A***, Experimental paradigm for visually guided swim assays. Training under photopic conditions consisted of 5 trials/d for 4 d. Test trials were subsequently done for 5 d in photopic conditions, followed by 5 d in scotopic conditions. Only 5 trials were conducted per day to prevent exhaustion of the animals. ***B***, Performance of animals during the training period. The time required to swim to the platform is plotted against training day. Mice that did not find the platform within 30 s on days 1 and 2 or 45 s on days 3 and 4 were guided manually to the platform. Unlike the other genotypes, which learned to find the platform within the training period, $Ca_v1.4$ KO mice continued to require assistance. ***C***, The average swim latency in 30 test trials is plotted for WT, $\alpha_2\delta$-4 HET, $\alpha_2\delta$-4 KO, $Ca_v1.4$ KO, and mGluR6 KO mice. Results are shown for photopic and scotopic conditions. Significant differences were determined by two-way ANOVA with Dunnett's *post hoc* test. ***B***, ***C***, Data are mean ± SEM. n.s., not significant ($p > 0.05$). ***$p \leq 0.001$. ****$p \leq 0.0001$.

neurotransmitter release (Dick et al., 2003; Reim et al., 2009). The partial sparing of cone ribbons in β_2-KO and $\alpha_2\delta$-4 KO mice may result from cone-specific mechanisms that help stabilize $Ca_v1.4$ channels at the developing active zone in the absence of β_2 or $\alpha_2\delta$-4.

While our study was under review, Wang et al. (2017) characterized their own $\alpha_2\delta$-4 KO mouse line, which had retinal phenotypes that are consistent with our observations. However, these authors did not find major abnormalities in cone synapse structure despite evidence from ERGs and patch-clamp recordings suggesting significant impairment of cone synaptic transmission in their $\alpha_2\delta$-4 KO mice (Wang et al., 2017). We discovered the structural defect in $\alpha_2\delta$-4 KO cone synapses by measuring cone bipolar sprouting (Fig. 4*C*,*D*) and through 3D reconstructions by serial block face scanning EM (Fig. 5). This latter strategy was particularly informative: even though ribbons were normally distributed throughout the pedicle (Fig. 5*A*), a minority of the $\alpha_2\delta$-4 KO cone ribbons were found within a synaptic triad (Table 2). Thus, imperfect wiring of cone synapses may contribute to abnormalities in cone transmission through ON and OFF bipolar pathways in our $\alpha_2\delta$-4 KO mice (Fig. 9) and in humans with $\alpha_2\delta$-4 mutations producing similar cone ERG phenotypes (Ba-Abbad et al., 2016). In this context, it is perhaps noteworthy that, with minor exceptions (i.e., rod ribbon length, Fig. 3*E*), WT and HET mice were similar with respect to the PR synapse properties investigated here. The significant differences noted in HET and $\alpha_2\delta$-4 KO mice (Figs. 2, 5, 6, 7; Fig. 5-1, available at https://doi.org/10.1523/JNEUROSCI.3818-16.2018.f5-1) may therefore parallel phenotypic distinctions between HET (unaffected) and homozygous individuals with cone-rod dystrophy due to CACNA2D4 mutations (Wycisk et al., 2006b; Ba-Abbad et al., 2016).

A major finding of the Wang et al. (2017) study was that $\alpha_2\delta$-4 interacts directly with the cell adhesion molecule, ELFN1, and forms a tertiary, trans-synaptic complex with mGluR6. The loss of rod synapses in both ELFN1 KO and $\alpha_2\delta$-4 KO mice supports a role for the $\alpha_2\delta$-4/ELFN1 interaction in rod synaptogenesis (Cao et al., 2015; Wang et al., 2017). However, ELFN1 is found at rod synapses and not cone synapses (Cao et al., 2015). Thus, there must be an additional mechanism by which $\alpha_2\delta$-4 regulates cone synapse structure. Consistent with our study, Wang et al. (2017) observed a profound reduction in presynaptic $Ca_v1.4$ channels in rods and cones, which we propose is the primary cause for the loss of rod and cone synapses in $\alpha_2\delta$-4 KO mice. First, PR synapse defects correlate with the extent to which presynaptic $Ca_v1.4$ channels are lost. Immunofluorescence for $Ca_v1.4$ is more strongly reduced in terminals of rods than cones at P10 an age when ribbons are readily found in cones and rarely in rods (Fig. 6; Table 3). The sprouting of rod and cone bipolar processes (Fig. 4) also parallels the disappearance of $Ca_v1.4$ immunofluorescence from PR terminals in $\alpha_2\delta$-4 KO (Fig. 6; Table 3), and a similar sprouting phenotype is seen in $Ca_v1.4$ KO mice (Raven et al., 2008; Liu et al., 2013; Zabouri and Haverkamp, 2013). The requirement for $Ca_v1.4$ in PR synapse development is further underscored by the findings of Wang et al. (2017) that electroporation of $\alpha_2\delta$-4 in rods of $Ca_v1.4$ KO mice does not rescue rod synapses (Wang et al., 2017). Finally, the loss of $Ca_v1.4$ channels in $\alpha_2\delta$-4 KO mice should disrupt a presynaptic network of proteins required for rod and cone synapse formation. These include bassoon and dystroglycan, the absence of which leads to impairments in ribbon maturation (Dick et al., 2003) and proper connectivity with bipolar cell processes (Omori et al., 2012). Collectively, the data support a model in which $\alpha_2\delta$-4 maintains the presynaptic density of $Ca_v1.4$ channels that serve as key organizers of rod and cone synapse assembly. Understanding the role of $Ca_v1.4$ in this process remains an important challenge for future studies.

References

Ba-Abbad R, Arno G, Carss K, Stirrups K, Penkett CJ, Moore AT, Michaelides M, Raymond FL, Webster AR, Holder GE (2016) Mutations in CACNA2D4 cause distinctive retinal dysfunction in humans. Ophthalmology 123:668–671.e2. CrossRef Medline

Bacchi N, Messina A, Burtscher V, Dassi E, Provenzano G, Bozzi Y, Demontis GC, Koschak A, Denti MA, Casarosa S (2015) A new splicing isoform of Cacna2d4 mimicking the effects of c.2451insC mutation in the retina: novel molecular and electrophysiological insights. Invest Ophthalmol Vis Sci 56:4846–4856. CrossRef Medline

Ball SL, Powers PA, Shin HS, Morgans CW, Peachey NS, Gregg RG (2002) Role of the β_2 subunit of voltage-dependent calcium channels in the retinal outer plexiform layer. Invest Ophthalmol Vis Sci 43:1595–1603. Medline

Ball SL, McEnery MW, Yunker AM, Shin HS, Gregg RG (2011) Distribution of voltage gated calcium channel beta subunits in the mouse retina. Brain Res 1412:1–8. CrossRef Medline

Bourdin B, Shakeri B, Tétreault MP, Sauvé R, Lesage S, Parent L (2015) Functional characterization of CaValpha2δ mutations associated with sudden cardiac death. J Biol Chem 290:2854–2869. CrossRef Medline

Buraei Z, Yang J (2013) Structure and function of the beta subunit of voltage-gated Ca^{2+} channels. Biochim Biophys Acta 1828:1530–1540. CrossRef Medline

Cao Y, Sarria I, Fehlhaber KE, Kamasawa N, Orlandi C, James KN, Hazen JL, Gardner MR, Farzan M, Lee A, Baker S, Baldwin K, Sampath AP, Martemyanov KA (2015) Mechanism for selective synaptic wiring of rod photoreceptors into the retinal circuitry and its role in vision. Neuron 87:1248–1260. CrossRef Medline

Caputo A, Piano I, Demontis GC, Bacchi N, Casarosa S, Della Santina L, Gargini C (2015) TMEM16A is associated with voltage-gated calcium channels in mouse retina and its function is disrupted upon mutation of the auxiliary α2δ-4 subunit. Front Cell Neurosci 9:422. CrossRef Medline

Cassidy JS, Ferron L, Kadurin I, Pratt WS, Dolphin AC (2014) Functional exofacially tagged N-type calcium channels elucidate the interaction with auxiliary α2δ-1 subunits. Proc Natl Acad Sci U S A 111:8979–8984. CrossRef Medline

Chang B, Heckenlively JR, Bayley PR, Brecha NC, Davisson MT, Hawes NL, Hirano AA, Hurd RE, Ikeda A, Johnson BA, McCall MA, Morgans CW, Nusinowitz S, Peachey NS, Rice DS, Vessey KA, Gregg RG (2006) The nob2 mouse, a null mutation in Cacna1f: anatomical and functional abnormalities in the outer retina and their consequences on ganglion cell visual responses. Vis Neurosci 23:11–24. CrossRef Medline

Cong L, Ran FA, Cox D, Lin S, Barretto R, Habib N, Hsu PD, Wu X, Jiang W, Marraffini LA, Zhang F (2013) Multiplex genome engineering using CRISPR/Cas systems. Science 339:819–823. CrossRef Medline

De Sevilla Müller LP, Liu J, Solomon A, Rodriguez A, Brecha NC (2013) Expression of voltage-gated calcium channel α2δ-4 subunits in the mouse and rat retina. J Comp Neurol 521:2486–2501. CrossRef Medline

Della Santina L, Kuo SP, Yoshimatsu T, Okawa H, Suzuki SC, Hoon M, Tsuboyama K, Rieke F, Wong ROL (2016) Glutamatergic monopolar interneurons provide a novel pathway of excitation in the mouse retina. Curr Biol 26:2070–2077. CrossRef Medline

Dick O, tom Dieck S, Altrock WD, Ammermüller J, Weiler R, Garner CC, Gundelfinger ED, Brandstätter JH (2003) The presynaptic active zone protein bassoon is essential for photoreceptor ribbon synapse formation in the retina. Neuron 37:775–786. CrossRef Medline

Dolphin AC (2016) Voltage-gated calcium channels and their auxiliary subunits: physiology and pathophysiology and pharmacology. J Physiol 594:5369–5390. CrossRef Medline

Fell B, Eckrich S, Blum K, Eckrich T, Hecker D, Obermair GJ, Münkner S, Flockerzi V, Schick B, Engel J (2016) α2δ-2 controls the function and trans-synaptic coupling of $Ca_v1.3$ channels in mouse inner hair cells and is essential for normal hearing. J Neurosci 36:11024–11036. CrossRef Medline

Hauke J, Schild A, Neugebauer A, Lappa A, Fricke J, Fauser S, Rösler S, Pannes A, Zarrinnam D, Altmüller J, Motameny S, Nürnberg G, Nürnberg P, Hahnen E, Beck BB (2013) A novel large in-frame deletion within the

CACNA1F gene associates with a cone-rod dystrophy 3-like phenotype. PLoS One 8:e76414. CrossRef Medline

Hoppa MB, Lana B, Margas W, Dolphin AC, Ryan TA (2012) $\alpha 2\delta$ expression sets presynaptic calcium channel abundance and release probability. Nature 486:122–125. CrossRef Medline

Huang J, Zhou L, Wang H, Luo J, Zeng L, Xiong K, Chen D (2013) Distribution of thrombospondins and their neuronal receptor alpha2δ1 in the rat retina. Exp Eye Res 111:36–49. CrossRef Medline

Jalkanen R, Mäntyjärvi M, Tobias R, Isosomppi J, Sankila EM, Alitalo T, Bech-Hansen NT (2006) X linked cone-rod dystrophy, CORDX3, is caused by a mutation in the CACNA1F gene. J Med Genet 43:699–704. CrossRef Medline

Katiyar R, Weissgerber P, Roth E, Dörr J, Sothilingam V, Garcia Garrido M, Beck SC, Seeliger MW, Beck A, Schmitz F, Flockerzi V (2015) Influence of the β_2 subunit of L-type voltage-gated cav channels on the structural and functional development of photoreceptor ribbon synapses. Invest Ophthalmol Vis Sci 56:2312–2324. CrossRef Medline

Knoflach D, Kerov V, Sartori SB, Obermair GJ, Schmuckermair C, Liu X, Sothilingam V, Garcia Garrido M, Baker SA, Glösmann M, Schicker K, Seeliger M, Lee A, Koschak A (2013) $Ca_v1.4$ IT mouse as model for vision impairment in human congenital stationary night blindness type 2. Channels 7:503–513. CrossRef Medline

Knoflach D, Schicker K, Glösmann M, Koschak A (2015) Gain-of-function nature of $Ca_v1.4$ L-type calcium channels alters firing properties of mouse retinal ganglion cells. Channels 9:298–306. CrossRef Medline

Lee A, Wang S, Williams B, Hagen J, Scheetz TE, Haeseleer F (2015) Characterization of Cav1.4 complexes ($\alpha_1$1.4, β_2, and $\alpha_2\delta$-4) in HEK293T cells and in the retina. J Biol Chem 290:1505–1521. CrossRef Medline

Liu X, Kerov V, Haeseleer F, Majumder A, Artemyev N, Baker SA, Lee A (2013) Dysregulation of $Ca_v1.4$ channels disrupts the maturation of photoreceptor synaptic ribbons in congenital stationary night blindness type 2. Channels 7:514–523. CrossRef Medline

Lock JT, Parker I, Smith IF (2015) A comparison of fluorescent Ca(2)(+) indicators for imaging local Ca(2)(+) signals in cultured cells. Cell Calcium 58:638–648. CrossRef Medline

Lodha N, Loucks CM, Beaulieu C, Parboosingh JS, Bech-Hansen NT (2012) Congenital stationary night blindness: mutation update and clinical variability. Adv Exp Med Biol 723:371–379. CrossRef Medline

Mansergh F, Orton NC, Vessey JP, Lalonde MR, Stell WK, Tremblay F, Barnes S, Rancourt DE, Bech-Hansen NT (2005) Mutation of the calcium channel gene Cacna1f disrupts calcium signaling, synaptic transmission and cellular organization in mouse retina. Hum Mol Genet 14:3035–3046. CrossRef Medline

Mashiko D, Fujihara Y, Satouh Y, Miyata H, Isotani A, Ikawa M (2013) Generation of mutant mice by pronuclear injection of circular plasmid expressing Cas9 and single guided RNA. Sci Rep 3:3355. CrossRef Medline

Masu M, Iwakabe H, Tagawa Y, Miyoshi T, Yamashita M, Fukuda Y, Sasaki H, Hiroi K, Nakamura Y, Shigemoto R (1995) Specific deficit of the ON response in visual transmission by targeted disruption of the mGluR6 gene. Cell 80:757–765. CrossRef Medline

Matsuda T, Cepko CL (2004) Electroporation and RNA interference in the rodent retina in vivo and in vitro. Proc Natl Acad Sci U S A 101:16–22. CrossRef Medline

McCall MA, Gregg RG (2008) Comparisons of structural and functional abnormalities in mouse b-wave mutants. J Physiol 586:4385–4392. CrossRef Medline

Mercer AJ, Thoreson WB (2011) The dynamic architecture of photoreceptor ribbon synapses: cytoskeletal, extracellular matrix, and intramembrane proteins. Vis Neurosci 28:453–471. CrossRef Medline

Omori Y, Araki F, Chaya T, Kajimura N, Irie S, Terada K, Muranishi Y, Tsujii T, Ueno S, Koyasu T, Tamaki Y, Kondo M, Amano S, Furukawa T (2012) Presynaptic dystroglycan-pikachurin complex regulates the proper synaptic connection between retinal photoreceptor and bipolar cells. J Neurosci 32:6126–6137. CrossRef Medline

Pang JJ, Chang B, Kumar A, Nusinowitz S, Noorwez SM, Li J, Rani A, Foster TC, Chiodo VA, Doyle T, Li H, Malhotra R, Teusner JT, McDowell JH, Min SH, Li Q, Kaushal S, Hauswirth WW (2006) Gene therapy restores vision-dependent behavior as well as retinal structure and function in a mouse model of RPE65 leber congenital amaurosis. Mol Ther 13:565–572. CrossRef Medline

Pérez de Sevilla Müller L, Sargoy A, Fernández-Sánchez L, Rodriguez A, Liu J, Cuenca N, Brecha N (2015) Expression and cellular localization of the voltage-gated calcium channel $\alpha 2\delta$-3 in the rodent retina. J Comp Neurol 523:1443–1460. CrossRef Medline

Prusky GT, West PW, Douglas RM (2000) Behavioral assessment of visual acuity in mice and rats. Vision Res 40:2201–2209. CrossRef Medline

Puthussery T, Gayet-Primo J, Taylor WR (2010) Localization of the calcium-binding protein secretagogin in cone bipolar cells of the mammalian retina. J Comp Neurol 518:513–525. CrossRef Medline

Raven MA, Orton NC, Nassar H, Williams GA, Stell WK, Jacobs GH, Bech-Hansen NT, Reese BE (2008) Early afferent signaling in the outer plexiform layer regulates development of horizontal cell morphology. J Comp Neurol 506:745–758. CrossRef Medline

Regus-Leidig H, Tom Dieck S, Specht D, Meyer L, Brandstätter JH (2009) Early steps in the assembly of photoreceptor ribbon synapses in the mouse retina: the involvement of precursor spheres. J Comp Neurol 512:814–824. CrossRef Medline

Regus-Leidig H, Specht D, Tom Dieck S, Brandstätter JH (2010) Stability of active zone components at the photoreceptor ribbon complex. Mol Vis 16:2690–2700. Medline

Regus-Leidig H, Atorf J, Feigenspan A, Kremers J, Maw MA, Brandstätter JH (2014) Photoreceptor degeneration in two mouse models for congenital stationary night blindness type 2. PLoS One 9:e86769. CrossRef Medline

Reim K, Regus-Leidig H, Ammermüller J, El-Kordi A, Radyushkin K, Ehrenreich H, Brandstätter JH, Brose N (2009) Aberrant function and structure of retinal ribbon synapses in the absence of complexin 3 and complexin 4. J Cell Sci 122:1352–1361. CrossRef Medline

Ruether K, Grosse J, Matthiessen E, Hoffmann K, Hartmann C (2000) Abnormalities of the photoreceptor-bipolar cell synapse in a substrain of C57BL/10 mice. Invest Ophthalmol Vis Sci 41:4039–4047. Medline

Schmitz Y, Witkovsky P (1997) Dependence of photoreceptor glutamate release on a dihydropyridine-sensitive calcium channel. Neuroscience 78:1209–1216. CrossRef Medline

Spiwoks-Becker I, Glas M, Lasarzik I, Vollrath L (2004) Mouse photoreceptor synaptic ribbons lose and regain material in response to illumination changes. Eur J Neurosci 19:1559–1571. CrossRef Medline

Tanimoto N, Akula JD, Fulton AB, Weber BH, Seeliger MW (2016) Differentiation of murine models of "negative ERG" by single and repetitive light stimuli. Doc Ophthalmol 132:101–109. CrossRef Medline

Thoreson WB, Nitzan R, Miller RF (1997) Reducing extracellular Cl^- suppresses dihydropyridine-sensitive Ca^{2+} currents and synaptic transmission in amphibian photoreceptors. J Neurophysiol 77:2175–2190. CrossRef Medline

Wang Y, Fehlhaber KE, Sarria I, Cao Y, Ingram NT, Guerrero-Given D, Throesch B, Baldwin K, Kamasawa N, Ohtsuka T, Sampath AP, Martemyanov KA (2017) The auxiliary calcium channel subunit alpha2δ4 is required for axonal elaboration, synaptic transmission, and wiring of rod photoreceptors. Neuron 93:1359–1374.e6. CrossRef Medline

Wycisk KA, Budde B, Feil S, Skosyrski S, Buzzi F, Neidhardt J, Glaus E, Nürnberg P, Ruether K, Berger W (2006a) Structural and functional abnormalities of retinal ribbon synapses due to Cacna2d4 mutation. Invest Ophthalmol Vis Sci 47:3523–3530. CrossRef Medline

Wycisk KA, Zeitz C, Feil S, Wittmer M, Forster U, Neidhardt J, Wissinger B, Zrenner E, Wilke R, Kohl S, Berger W (2006b) Mutation in the auxiliary calcium-channel subunit CACNA2D4 causes autosomal recessive cone dystrophy. Am J Hum Genet 79:973–977. CrossRef Medline

Zabouri N, Haverkamp S (2013) Calcium channel-dependent molecular maturation of photoreceptor synapses. PLoS One 8:e63853. CrossRef Medline